Implementation of optical depth scanning and wide-field imaging in photoacoustic remote sensing (PARS) microscopy

by

Lyazzat Mukhangaliyeva

A thesis
presented to the University of Waterloo
in fulfillment of the
thesis requirement for the degree of
Master of Applied Science
in
Systems Design Engineering

Waterloo, Ontario, Canada, 2022

Author's Declaration

I hereby declare that I am the sole author of this thesis. This is a true copy of the thesis, including any required final revisions, as accepted by my examiners.

I understand that my thesis may be made electronically available to the public.

Abstract

Optical resolution photoacoustic microscopy (OR-PAM) is a hybrid biomedical imaging technique that utilizes acoustic detection and optical absorption contrast. It is based on the photoacoustic effect, where the excitation light energy absorbed by biomolecules is converted into heat. The initial temperature rise causes thermo-elastic expansion in tissues, resulting in the generation of acoustic waves detected by an ultrasound transducer. OR-PAM takes advantage of tightly focused light as the excitation source to achieve micron to submicron optical lateral resolution at superficial depths (~1mm). Additionally, it provides high contrasts to endogenous chromophores allowing for label-free *in-vivo* imaging. As a result, OR-PAM is a powerful tool for morphological, functional, and molecular imaging of biological organisms and their vital processes. However, conventional OR-PAM architectures are usually limited by the need for an ultrasound transducer to be in direct contact with the sample through a coupling medium. This condition introduces complexity to optical design and implementation and might become a source of infection or contamination in applications where physical contact is undesirable or impossible.

Photoacoustic remote sensing (PARS) microscopy is an all-optical, label-free technique first introduced in 2017. But unlike OR-PAM, PARS does not require physical contact with the sample. PARS microscopy employs an interrogation beam as an alternative to the conventional ultrasonic transducer. There are, however, two limitations to PARS that will be addressed in this thesis dissertation. Firstly, PARS lacks an inherent 3D imaging capability since photoacoustic pressures induced by pulsed lasers are detected at their origin. Instead, volumetric imaging is achieved by mechanical scanning, which presents some drawbacks, such as slow scanning rates and motion artifacts, as well as being bulky and expensive. Optical focus shifting may allow PARS to image larger volumes at higher speeds and with higher resolution.

In this work, a novel continuous micro-electromechanical systems (MEMS) deformable mirror (DM) was integrated into a PARS microscope for imaging at varying depths. The first step was to create an optical model using the DM characteristics and use Zemax to predict the focal shift. Next, an experimental investigation of the focus shifting ability of the DM was conducted using a 532-nm scattering microscope, and a focal shift of 240 μm was achieved. Afterward, carbon fiber imaging was conducted to demonstrate the axial scanning capabilities of DM-based PARS microscopy. Lastly, the focal plane was optically shifted to perform *in-vivo* PARS imaging of blood vessels in chick embryo chorioallantoic membrane (CAM) models at different depths.

The second limitation of PARS microscopy is its inability to provide fast wide field of view (WFOV) imaging. WFOV imaging is achieved by mechanically scanning small areas laterally at different positions and then stitching them together. Mechanical scanning, however, is slow, prone to motion artifacts, and might agitate sensitive samples. As part of this work, we demonstrated how an optical approach using a scan lens could be used to achieve 8.5×8.5 mm^2 FOV imaging of carbon fibers in PARS. Moreover, the system was utilised in *in-vivo* studies by imaging CAM vasculature and reaching up to 3.34×3.34 mm^2 FOV. Further system enhancements are needed to expand the FOV, increase imaging speeds, and improve resolution. This potentially can be realized by integrating adaptive optics elements to actively correct for system- and specimen-induced aberration and adjust focus over a large FOV.

Acknowledgements

First of all, I would like to thank my co-supervisor, Dr. Parsin Haji Reza, for seeing my potential the very first time we met and giving me a chance to restart my career. Thank you for teaching me to always strive for excellence and be dedicated to the work I do.

Next, I would like to thank my co-supervisor, Prof. Eihab Abdel-Rahman, for always believing in me, encouraging me, and supporting me at every step. You have taught me to always stay humble, positive, and true to myself. And as a member of your research group, I have always felt welcomed and accepted.

I would like to thank Marian Boktor, Alkris Warren, Samed Kocer, and Layla Khalili for always believing in me, assisting me with experiments, staying late in the labs, and always listening to me. Thank you for always accepting and sharing my achievements and failures, tears and laughter, joys and sorrows. You guys are amazing, and I will always be grateful for your support.

My master's wouldn't have been as enjoyable without other graduate students and lab members. Thanks for all the support, guidance, and fun throughout my masters: Ben Ecclestone, Nima Abbasi, Stephanie Clarke, Kevan Bell, Hager Gouda, Zohreh Hosseinaee, Alex Tummon Simmons, James Tweel, Tara Amiri, Nicholas Pellegrino, and Krystal Li.

Last but not least, I would like to thank Jean Flannagan and Nancy Gibson for always helping us with our experiments and having heartwarming conversations.

Dedication

To my beloved family! I love you so much!

Table of Contents

List of Figures

List of Tables

List of Abbreviations

AO	Adaptive optics
AOSLO	Adaptive optics scanning laser ophthalmoscopy
APD	Avalanche photodiode
BC	Beam condenser
CAM	Chorioallantoic membrane
CCD	Charge-coupled device
DM	Deformable mirror
ESF	Edge spread function
FOV	Field of view
FWHM	Full width at half maximum
GRIN	Gradient index
GV	Galvanometer
IPA	Isopropyl alcohol
LC	Liquid crystal
LL	Liquid lens
LSF	Line spread function
MEMS	Micro-electromechanical systems
NA	Numerical aperture
NIR	near-infrared
OCT	Optical coherence tomography
OL	Objective lens
OPL	Optical path length
PAM	Photoacoustic microscopy
PARS	Photoacoustic remote sensing
PBS	Polarizing beam splitter
PRR	Pulse repetition rate
QWP	Quarter-wave plate
SF	Spectral filter
SHWS	Shack-Hartmann wavefront sensor

SLM	Spatial light modulator
SNR	Signal-to-noise ratio
SO_2	Oxygen saturation
TA	total absorption
TLCL	Tunable liquid crystal lenses
UHR	Ultra-high resolution
USAF	United States Air Force
UV	Ultra-violet
WFOV	Wide field of view
WS	Wavefront sensor
ZC	Zoom collimator

Chapter 1: Background

1.1 Introduction

Optical imaging is a powerful technique that uses light to observe, image, and study a wide range of biological structures, from molecules to organs and their vital functions. Prime examples of optical imaging include but are not limited to photoacoustic imaging, white-light endoscopy methods, optical coherence tomography (OCT), and Raman spectroscopy.

One significant advantage of optical imaging is that it uses non-ionizing radiation, which reduces harmful exposure to a substantial extent and allows for repeated use to monitor the progression of a disease, drug delivery, or assess the outcome of treatment [1]. Moreover, optical imaging has a high spatial resolution, high soft tissue contrast, fast data acquisition speed, and is relatively inexpensive, making it an excellent alternative to other imaging techniques. By using optical imaging in conjunction with other imaging techniques, physicians and researchers can better understand complex diseases and conduct elaborate experiments using more detailed information.

Despite this, many factors influence the quality of an image. Standard imaging modalities can be enhanced to be more efficient and effective with the use of high-quality optical components. However, even with a nearly perfect diffraction-limited microscope and perfect alignment, images can still be distorted by specimen-induced aberrations resulting from a refractive index mismatch between the sample and the medium or field-dependent refractive index variation within the sample itself [2]. Optical aberrations also result in a substantial reduction of the depth of imaging to a few cellular layers just beneath the surface [3]. Nevertheless, it is crucial for biomedical research to be able to image biological structures and processes on a molecular level deep within their natural environment and not on a microscope slide. Implementing adaptive optics (AO) is one way to minimize aberrations. This add-on technology manipulates the optical wavefront to correct system- or specimen-induced

aberrations [4]. Significant progress has been made in the field of AO in the past twenty years. Adaptive optics elements were integrated into a wide range of modalities in the most creative ways to address the issues of conventional setups. The purpose of this chapter is to provide a brief overview of the history and components of AO, as well as discuss the theory of aberrations. In Chapter 2, the current applications of AO are examined in greater depth, specifically for aberration correction and depth scanning purposes.

1.2 A Brief History of Adaptive Optics

The first telescope was invented in the early 17th century. Astronomers soon realized that atmospheric turbulence limited their ability to observe the sky. Capturing images from the top of the tallest mountains significantly reduced the blurriness, but the images were still far from perfect. The only way to acquire high-resolution images of celestial bodies was to send the telescope into space, which was a costly option.

Horace Babcock first introduced the concept of AO in 1953 [5]. The idea was to measure wavefront aberration caused by atmospheric turbulence and then compensate for it by using a wavefront corrector. Unfortunately, due to the state of technology at that time, its implementation was impossible. It was not until the advance of computer technology in the 1990s that this technology was made practical for use in astronomy. However, evidence suggests that early adaptive optics research was conducted in the 1970-1980s too, but with restricted use. Thus, early AO components such as detectors, deformable mirrors, and reconstructors were developed. One of the very first AO-based projects was called COME-ON. It incorporated a 19-actuator deformable mirror and a 20-subaperture Shack–Hartmann wavefront sensor with a 32×32 pixel near-infrared (NIR) imager [6]. The following years saw the development of many types of AO-based telescopes.

In the early 2000s, AO entered a new development phase, becoming a primary scientific driver and producing high-impact astronomical findings. Moreover, AO has found its place in biomedical research. It is now a popular add-on technique for medical imaging applications, such as retinal and deep tissue imaging.

1.3 Components of AO

Light is a form of energy that has both particle and wave properties. The way light travels in straight lines can be explained by its particle nature (called a photon). The way light bends and diffracts around objects is explained by its wave-like behavior. Let's take a point source that emits light in all directions. The tips of rays with constant optical path lengths (OPL) and constant phase will lie on the surface of a sphere, as shown in Figure 1-1. This imaginary surface is called a wavefront and sometimes is referred to as a phasefront. Wavefront is always normal to the rays of light [7].

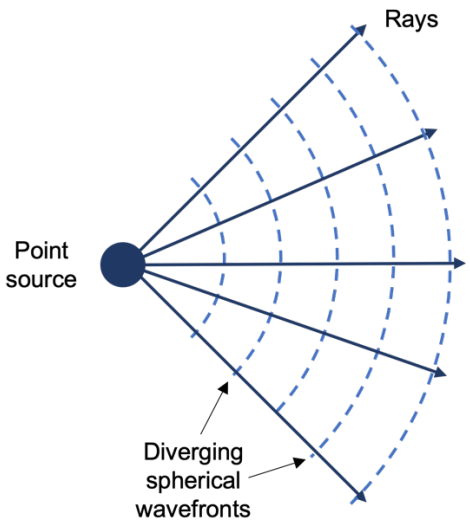

Figure 1-1. Spherical wavefronts representation.

However, it is essential to mention that a wavefront is not always spherical. Essentially, wavefronts can be divided into three main types: plane wavefronts, spherical wavefronts, and

cylindrical wavefronts. For example, a point source located at infinity produces flat wavefronts with constant phase and OPL.

In AO, there are three main components: a wavefront sensor (WS) to measure distortion, a wavefront corrector to compensate for distortion, and a control system to calculate and apply the corrections. Figure 1-2 illustrates the principle of a classical AO system. In this case, a deformable mirror reflects the light from the telescope, which is then sent directly to a high-resolution camera. A small portion of it, however, is split and directed to a wavefront sensor. Then, the shape of the deformable mirror is changed according to the wavefront analysis and corrections calculated. As a result of the change in the mirror shape, the camera now receives a newly corrected wavefront free of aberrations. It is crucial to keep in mind that the architecture of the AO can vary greatly depending on the application.

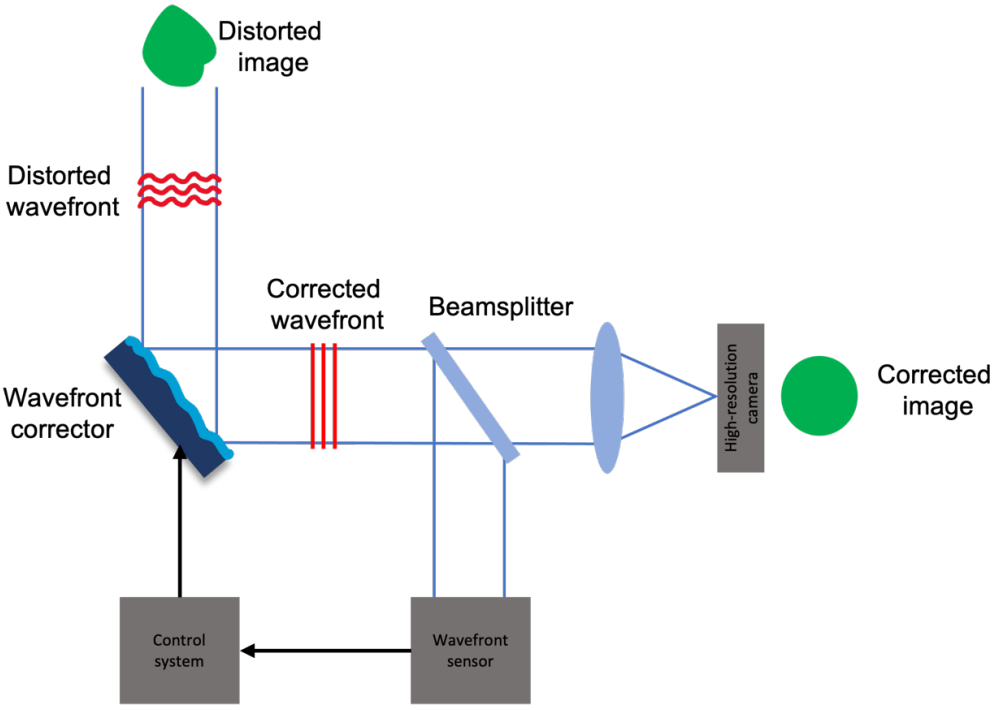

Figure 1-2. Principle of AO in a closed-loop arrangement.

1.3.1 Wavefront Sensors

Optical wavefront sensing is essential to understanding optical quality and developing advanced wavefront correction techniques. Different wavefront sensors are available, including Shack-Hartmann WS, shearing interferometers, pyramid sensors, and curvature sensors. The following properties should be considered when choosing the most suitable wavefront sensors: sensitivity, linearity, achromaticity, dynamic range, spatial aliasing, computational requirements, and ease of implementation [6]. For these reasons and its simplicity and ease of manufacture, Shack-Hartmann WS (SHWS) is the most commonly used wavefront sensor.

In a SHWS, an array of lenslets samples the wavefront to form spot images onto a detector. For an unaberrated wavefront, the focal spots will be formed precisely at the reference position of the detector, as shown in Figure 1-3A. On the other hand, with an aberrated wavefront, the location of the focused spot on the detector changes depending on the magnitude of the local tip-tilt component of aberration, Figure 1-3B. Therefore, the location of the focal spots on a detector is used to reconstruct and analyze the wavefront shape using Zernike polynomials [8]. Furthermore, SHWS's high sensitivity, achromaticity, and linearity make it the ideal choice for many applications.

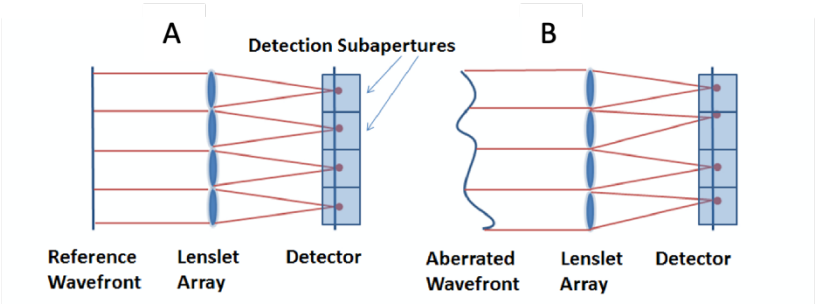

Figure 1-3. Basic operating principle of a conventional Shack-Hartmann Wavefront Sensor (A) Collimated reference wavefront and (B) Aberrated wavefront. [8]

This device has a disadvantage because it requires precision when aligning and calibrating. In addition, vibrations or distortions in the optics can affect the spot positions, resulting in inaccurate wavefront slope measurements. SHWS has another disadvantage: a large charge-coupled device (CCD) camera is required to achieve high spatial resolution, which can be costly and bulky [3].

Shearing interferometers are another type of wavefront sensing devices. They test coherent light beams for collimation based on interference measurement. The name shearing interferometer comes from its main component, the shear plate. N-BK7 optical glass is typically used for shearing plates. It is usually best to place the shear plate at a 45° angle to obtain maximum sensitivity. When a plane wave is incident on a shear plate, it gets reflected twice, as shown in Figure 1-4. These two wavefronts are combined to produce constructive and destructive interference. A light fringe occurs when parts of the wavefront are in phase, while a dark fringe occurs when they are out of phase.

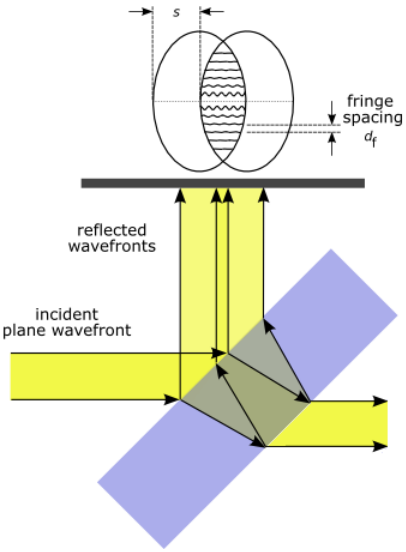

Figure 1-4. View of a shear plate and the resulting interference pattern. [9]

1.3.2 Wavefront correctors

In adaptive optics, wavefront correctors are crucial to restoring image quality by reshaping wavefronts. DMs and spatial light modulators (SLMs) are the two main types of wavefront correctors. The commercial market now offers a wide variety of these correction devices that are both affordable and practical. However, since both wavefront correctors have their advantages and disadvantages, one should carefully select the device that will work best for their system based on the desired results.

An SLM is a device that modulates the amplitude, phase, or polarization of light waves in space and time. It is possible to control these parameters separately or in combination. SLMs can be operated either in reflection or transmission modes. SLMs are either electrically or optically addressed depending on their driving signal. It is common for SLMs to have a slow refresh rate of 100 Hz or lower. As wavelength increases, refresh rates decrease even further as device thickness increases. SLMs are a great choice for specific applications because they are easy to use, have a high resolution, offer flexibility during operation, and produce a greater variety of patterns due to their number of pixels [10],[11].

There are many types of DMs based on their surface structure, actuation method, surface layer, and electrode count. Based on the DM's surface structure, for instance, it can be continuous or segmented, as demonstrated in Figure 1-5. Actuation methods for DMs can be electrostatic, electromagnetic, or piezoelectric.

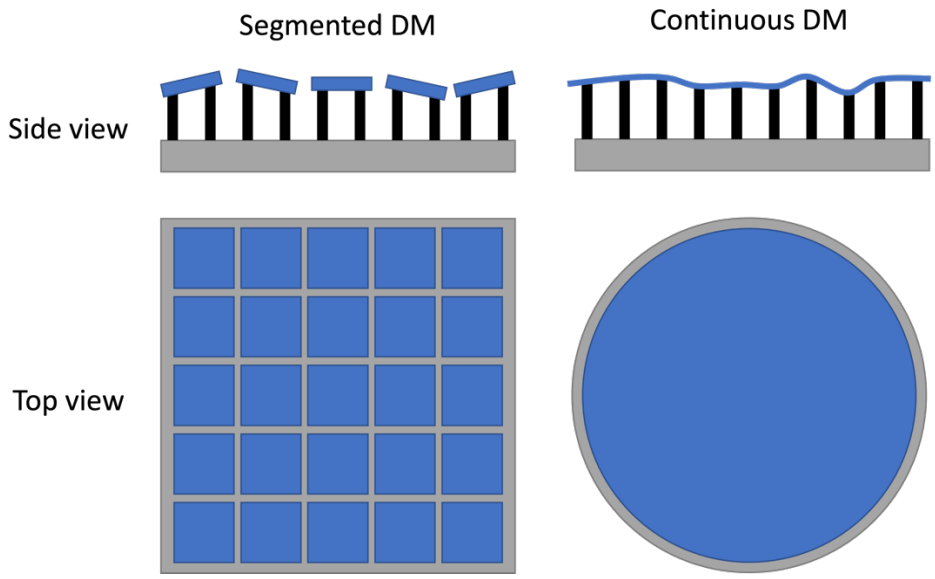

Figure 1-5. Different types of DMs based on the surface structure.

Stroke is a crucial aspect of DMs that describes how much displacement can be achieved at the mirror surface coating (e.g., gold, aluminum, protected silver, etc.) A stroke can vary from a few micrometers to tens of micrometers, but for microscopy, vision science, and laser shaping, 1-4 μm of stroke is usually enough [12]. Stroke can be calculated using the following formula:

$$Stroke = (0.5)(5)(1.2)\sqrt{\mu}\left(\frac{D}{r_0}\right)^{5/6} \quad (1)$$

where D is the diameter of the mirror, r_o is the coherence length, and μ is a fitting coefficient that depends on the type of the mirror.

With the help of microelectromechanical systems (MEMS) technology, deformable mirrors have become more cost-effective and high-performance than ever. As a result of electrostatic actuation, MEMS DMs can achieve subnanometer precision, operate at higher repetition rates (kHz), and are cost-effective [13]. In addition, they are usually lightweight, wavelength-independent, and mechanically robust. The field of AO has seen massive growth in the past 20 years due to the advantages of DMs mentioned above, particularly their reliability and low cost. However, any device has its drawbacks,

and DMs are no exception. Some of their shortcomings are small apertures (many applications require large apertures), limited coating choices, poor surface quality, and difficulty in controlling high voltages on a micro-scale [14].

1.4 Aberrations

Understanding aberrations and how they affect imaging quality is essential for understanding AO and implementing it in a system. A short introduction to the theory behind aberrations and Zernike polynomials is provided in this section [2].

Several common aberrations have been well studied and can be corrected with carefully designed optics, including spherical, chromatic, coma, and astigmatism. However, it is more complex to analyze sample-induced aberrations caused by spatial variations in the refractive index; their magnitudes can range significantly from one field of view to another. The definition of aberration will be examined in more detail here.

Based on the Snell's law of refraction, we can describe the absolute phase of a point at the location L(x,y,z) within the optical system's beam path with respect to the focal point as:

$$\Phi\big(L(x,y,z)\big) = \int_f^{L(x,y,z)} \frac{2\pi}{\lambda} n(\tilde{x},\tilde{y},\tilde{z})dw \tag{2}$$

where λ is the wavelength, w is the traveled distance, f is the focal length, and $n(\tilde{x},\tilde{y},\tilde{z})$ is the variation in the refractive index. The aberration function in the pupil plane of the lens can be defined as follows:

$$\Psi(x,y) = \int_f^{P(x,y,z_o)} \frac{2\pi}{\lambda} \left(n(\tilde{x},\tilde{y},\tilde{z}) - n_o(\tilde{x},\tilde{y},\tilde{z})\right) dw \tag{3}$$

where z_o is the axial position of the pupil plane, $n_o(\tilde{x},\tilde{y},\tilde{z})$ is the refractive index distribution function of the ideal case, and $n(\tilde{x},\tilde{y},\tilde{z})$ is the refractive index distribution function of the aberrated case.

1.5 Zernike polynomials

Zernike polynomials represent a convenient way to describe aberrations present in the optical setup. There are odd and even Zernike polynomials [2]. Even Zernike polynomials are defined as:

$$Z_n^m(r,\theta) = R_n^m(r)\cos(m\theta) \tag{4}$$

and the odd Zernike polynomials are defined as

$$Z_n^{-m}(r,\theta) = R_n^m(r)\sin(m\theta) \tag{5}$$

where m and n are nonnegative integers, r is the radial distance normalized to the range from 0 to 1, and R_n^m is the radial polynomial defined as:

$$R_n^m(r) = \sum_{k=0}^{\frac{n-m}{2}} \frac{(-1)^k(n-k)!}{k!\left(\frac{n+m}{2}-k\right)!\left(\frac{n-m}{2}-k\right)!} r^{n-2k} \tag{6}$$

Zernike polynomials range from -1 to 1. Figure 1-6 represents 15 orders of Zernike modes. However, there are many more. These modes can be combined to describe the wavefront of the beam.

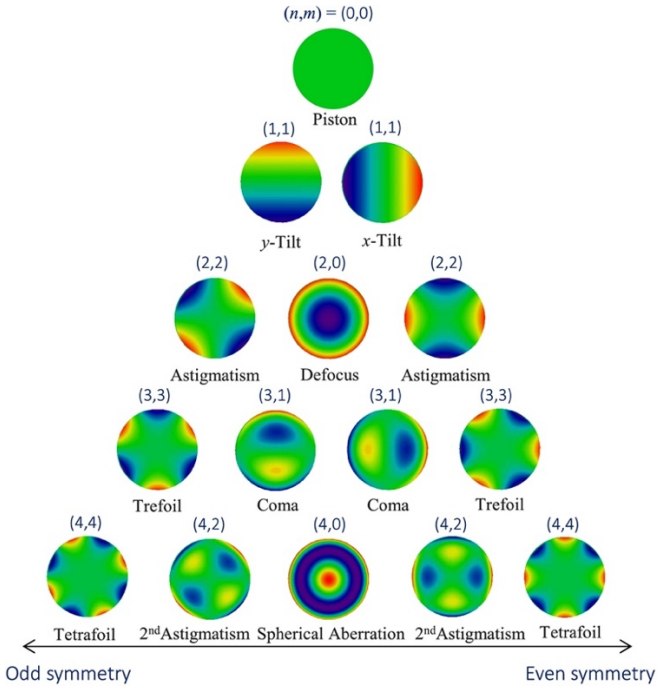

Figure 1-6. Zernike polynomials and corresponding aberrations [15].

The wavefront aberration over the normalized pupil of the system can be calculated in radians as:

$$\Psi(r,\theta) = \sum_{i=1}^{\infty} M_i Z_i(r,\theta) \quad (7)$$

where M_i are the modal coefficients that describe the strength of the Zernike polynomial and are defined as follows:

$$M_i = \frac{1}{\pi}\int_0^1 \int_0^{2\pi} \Psi(r,\theta)\, Z_i(r,\theta) r dr d\theta \quad (8)$$

1.6 Photoacoustic remote sensing microscopy and its applications

One imaging modality where implementing AO might be promising is photoacoustic remote sensing (PARS) microscopy. The first report on PARS microscopy was published by Haji Reza *et al.* in 2017 [16]. As PARS microscopy is based on photoacoustic microscopy, understanding photoacoustic microscopy is essential.

Photoacoustic microscopy is a hybrid imaging technique that relies on optical absorption contrast and acoustic detection [17]. It is based on the photoacoustic effect, where the excitation light energy absorbed by biomolecules is converted into heat. The initial temperature rise causes thermo-elastic expansion in tissues, resulting in the generation of acoustic waves detected by an ultrasound transducer [18]. Since acoustic waves scatter less than light in biological tissues, photoacoustic microscopy represents an attractive modality for high-resolution imaging at greater depths than purely optical approaches [19]. However, a significant drawback of conventional photoacoustic microscopy is the requirement for an ultrasound transducer to be in direct physical contact with the sample through a coupling medium [20]. Such contact increases the risk of infection and contamination in open wound diagnostics and can result in microscopic injuries and patient discomfort in ophthalmic applications [21][22]. These complications make transducer-based photoacoustic techniques undesirable in many clinical and pre-clinical applications.

PARS is a novel form of photoacoustic microscopy that does not require contact and replaces a traditional ultrasonic transducer with an interrogation beam. PARS microscopy involves co-focusing and co-aligning the two beams, excitation and interrogation, on a sample. In the excitation process, chromophores absorb energy, which is then converted into pressure by thermo-elastic expansion. As pressure increases, local optical properties within absorbers undergo elasto-optic modulations. As a result, the intensity of the back-reflected interrogation beam changes. Currently, gel-based tissue phantoms can be imaged with PARS to a depth of 2.5 mm [23]. In situations such as endoscopy or surgery, where contact with the specimen is not desired or the working space is limited, PARS can be especially useful. Moreover, remote detection minimizes contamination risks, tissue deformation from contact, and patient discomfort *in-situ*. Lastly, due to the all-optical nature of PARS, it can also easily be integrated with other imaging modalities.

PARS offers chromophore-specific contrast by targeting the unique absorption spectra of biomolecules with different excitation wavelengths. For example, DNA/RNA-containing structures are targeted by UV excitation light [24][25], while hemoglobin is targeted by visible light around 500 nm [26].

Research has proven that PARS has the potential to be a better alternative to conventional histopathology visualization practices by solving their limitations, such as lengthy staining processes and dye usage. Boktor *et al.* [27] used total-absorption (TA-PARS) images of unstained tissue to generate a virtual stain-free histochemical staining method using a deep-learning-based approach. As illustrated in Figure 1-7, the scientists' virtually stained images of unstained skin tissues are very similar to the ground truth images obtained through conventional H&E staining. Since the primary goal of PARS in histology is to image freshly resected tissues without processing them first, this imaging technique may eventually be integrated into an advanced surgical microscope to assist surgeons in

resecting cancer. PARS might substantially reduce the time and resources required for conventional tissue processing and imaging.

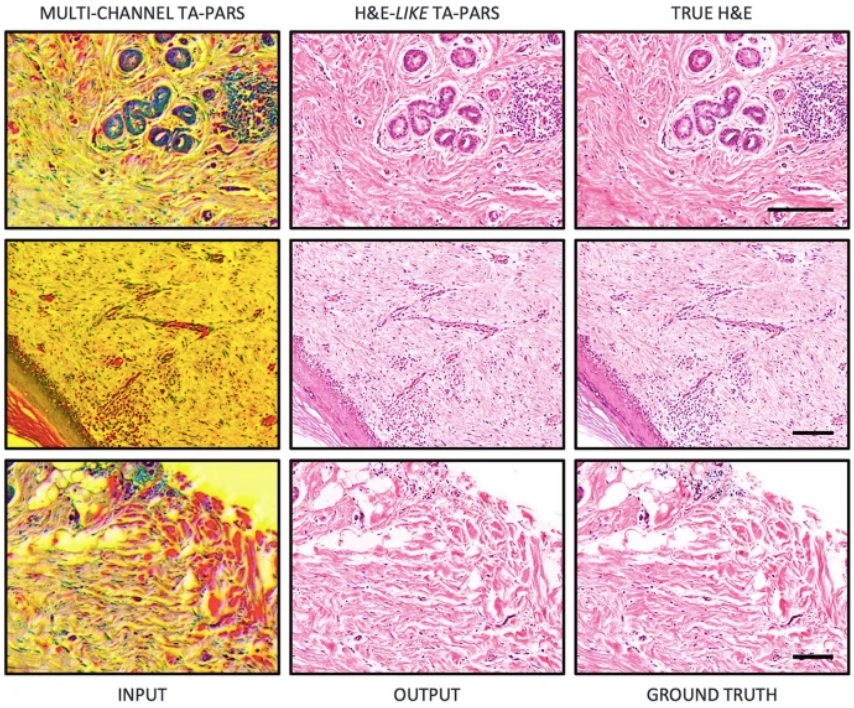

Figure 1-7. Virtual staining of TA-PARS images of human skin tissue slides. Scale bar:100 µm [27]

In ophthalmology, the most prevalent blinding diseases can be diagnosed earlier by analyzing functional changes before structural changes become noticeable. In this situation, PARS would be a beneficial tool to accurately measure ocular blood flow to capillaries, oxygen saturation, and metabolic rate of oxygen. In their research, Hosseinaee *et al.* [28] successfully acquired images of rat eye ocular tissue, as depicted in Figure 1-8. In addition, a corresponding oxygen saturation (SO_2) map was also obtained using multiwavelength PARS.

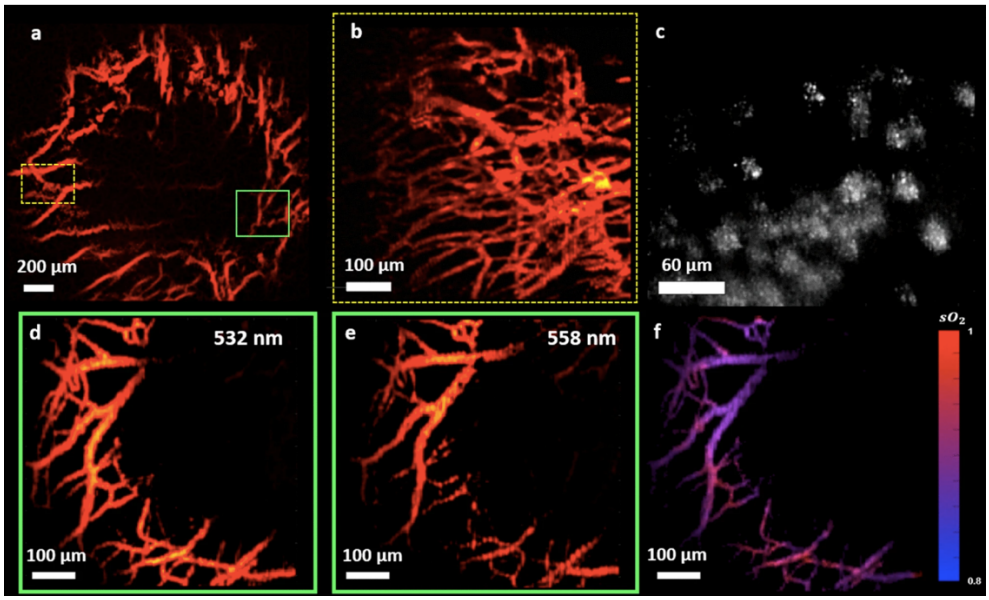

Figure 1-8. In-vivo imaging of ocular tissue using PARS.
(a) Vasculature of the iris imaged from ~ 2.5 mm × 2.5 mm area. (b) Vasculature around the iris imaged with PARS. (c) In-vivo images of melanin content in the retinal pigment epithelium and choroid layers. (d) Images acquired using a multiwavelength PARS system at 532 nm (e) 558 nm and (e) the corresponding SO_2 map. [28]

PARS can be further developed with many valuable features and functionalities. PARS, for example, is not an interferometric technique like optical coherence tomography (OCT). As opposed to PAM, PARS does not detect photoacoustic time-of-flight. Instead, it detects the photoacoustic pressures induced by pulsed lasers at their source, which means it isn't an intrinsic 3D imaging system. In conventional PARS microscopy architectures, two-dimensional data is acquired, and volumetric imaging is performed via mechanical scanning [29][30]. Mechanical scanning has many disadvantages that will be discussed in more detail in Chapter 3, along with a proposed solution – optical focus shifting.

Last but not least, PARS microscopy achieves a wide field of view imaging through mechanical scanning. Even though this method is widely used, certain applications require a faster method that does not physically move the sample. Initial stages of research toward WFOV PARS microscopy using a scan lens for optical scanning are presented in Chapter 4.

Chapter 2: Current applications of adaptive optics

The performance of optical microscopes can be negatively affected by aberrations originating from imperfect optics, system misalignment, or specimens. Specimen-induced aberrations can be further categorized into field-dependent refractive index variation within the specimen and refractive index mismatch between the specimen and the immersion medium [2]. AO can effectively correct these aberrations, restoring diffraction-limited imaging capabilities. Over the past 20 years, AO has been rapidly developing. For example, AO correction is nowadays essential to visualize three-dimensional neural structures in the brain with enhanced resolution. Though it has been implemented with many imaging modalities, there is still a lot of room for improvement. The demand for compact, lightweight, fast, easy-to-use, affordable AO technology is high. However, AO is also not limited to aberration correction and can be applied to various other applications. Chapter 2 examines how scientists have used AO for aberration correction and depth scanning.

2.1 Aberration correction applications

The tip/tilt correction in a transmission confocal microscope was one of the first applications of adaptive optics in microscopy [31]. In this case, structures in the specimen shift the spot at the detector laterally. In order to ensure that the focal spot on the detector remains unchanged, a tilting mirror was proposed. Researchers have demonstrated that tip-tilt mirrors can remove motion in real-time imaging and post-processing of CCD images. They have also investigated the correction of other low-order aberrations requiring a wavefront sensor and a wavefront corrector.

During confocal microscopy, both illumination and fluorescence lights pass through the specimen. It is, therefore, inevitable that both paths will have aberrations. Aberration correction must be performed in both paths to achieve diffraction-limited operation. An example of this dual path aberration correction using a DM in confocal microscopy imaging of a fluorescently labeled section of

mouse intestine specimen is shown in Figure 2-1 [32]. Image dimensions are 80×80×15 μm in the x, y, and z directions, respectively.

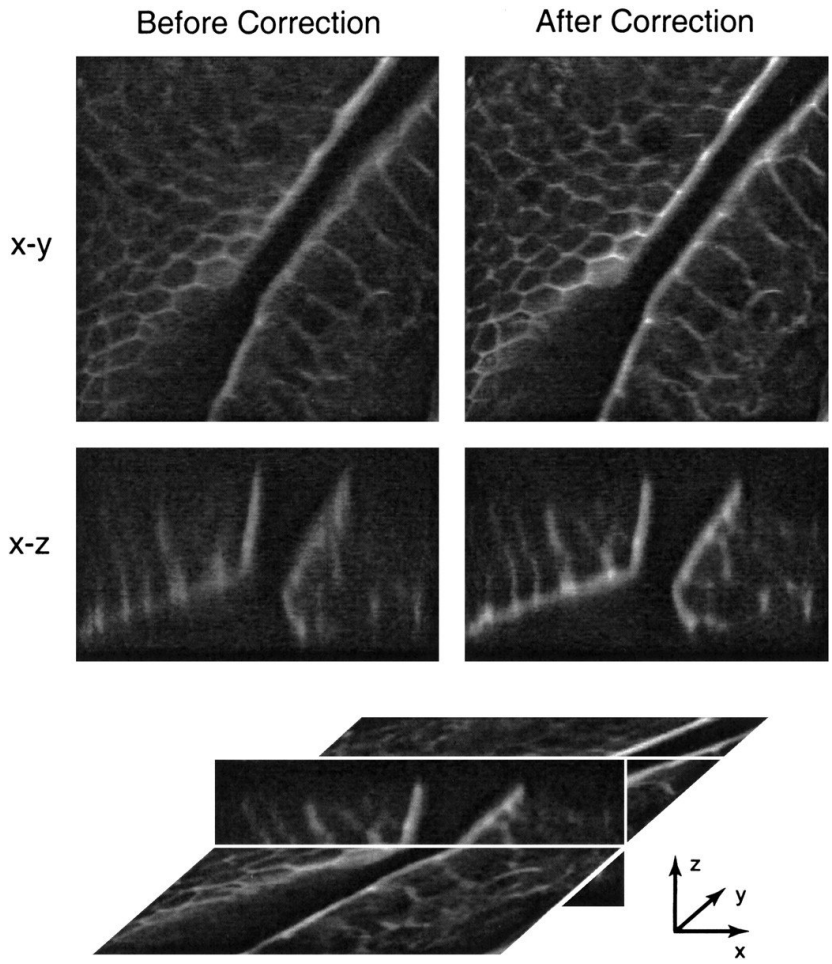

Figure 2-1. Confocal microscope scans before and after aberration correction.
x-y (lateral) and x-z (axial) scans of a fluorescently labeled section of mouse intestine specimen. [32]

On the other hand, two-photon microscopy does not usually use a pinhole detector; hence, aberrations in the detection path don't impair resolution or signal strength. Thus, the illumination path is the only part of a two-photon microscope that requires aberration correction. There has been much work done on implementing these kinds of systems using DMs [33], [34] and liquid crystal SLMs [35], [36].

AO has also been successfully implemented with two main OCT techniques: time-domain OCT and Fourier domain OCT. Hermann *et al.* [37] demonstrated the use of adaptive optics ultra-high resolution (AO-UHR) OCT for the first time in *in-vivo* retinal imaging. They utilized a 37-actuator membrane deformable mirror, a real-time Hartmann–Shack wavefront sensor operating at 30 Hz, a compact Ti:sapphire laser with 130-nm bandwidth, and the footprint of the system was 300 mm×300 mm. This AO-UHR OCT resulted in high axial (3 μm) and improved transverse resolution (5–10 μm). With the help of AO, they were able to correct for ocular and system aberrations for a 3.68 mm input beam diameter. They have also improved the signal-to-noise ratio (SNR) by up to 9 dB in the AO-corrected images.

Wong *et al.* [38] demonstrated *in-vivo* imaging of human photoreceptor mosaic wavefront sensorless AO-OCT (WSAO-OCT). This imaging system successfully replaced the Shack-Hartmann wavefront sensor with a depth-resolved image-driven optimization algorithm based on real-time volumes acquired by OCT. As a result, WSAO-OCT is compact, low-cost, and robust for clinical high-resolution retinal imaging applications. The achievable transverse resolution was 2.76 μm. They validated the performance of the system by imaging the retina at several eccentricities, as can be seen in Figure 2-2 below.

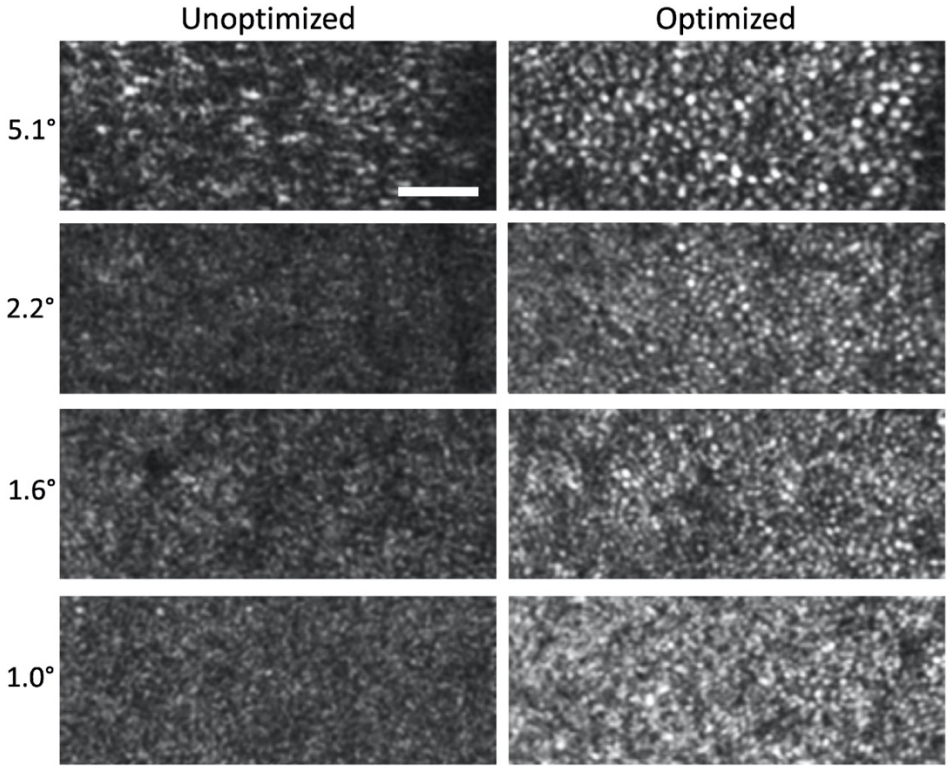

Figure 2-2. Photoreceptor mosaic images acquired along the superior meridian in a non-mydriatic pupil. These include results acquired at four retinal eccentricities for comparison centered at: 5.1°, 2.2°, 1.6°, and 1.0°. The field of view is 1.0°x0.4° for all images. Scale bar is 50 µm. [38]

Micro-endoscopy is another area in which the use of aberration-correcting optics (AO) could make a significant contribution to the field of medical imaging. Due to their small dimensions, such systems present an optical design challenge for three-dimensional imaging. In order to build these endoscopes, graded index (GRIN) rod lenses can be used, but they have only one free parameter in their design, which is the radial refractive index profile. As a result, optimizing the system's on-axis performance is always possible, but significant aberrations occur when the field of view extends beyond the center. To address these issues and improve the imaging performance of endoscopes, researchers introduced AO. For example, the use of adaptive fiber bundle endoscopes with SLMs for beam scanning and aberration correction has been investigated [39]. In another study, Bortoletto *et al.* [40] incorporated a GRIN fiber objective into a multiphoton confocal fluorescence microscope and corrected

aberrations with an electrostatic membrane mirror. A test of the adaptive system was conducted on 1μm fluorescent microspheres, and as shown in Figure 2-3, the image quality was greatly improved.

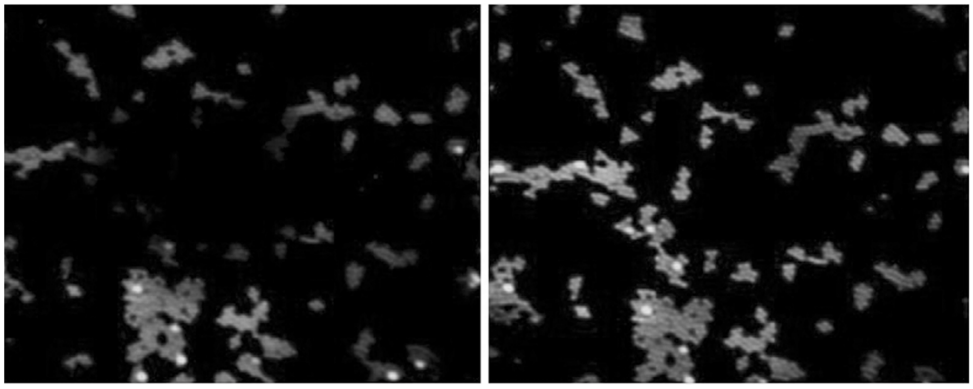

Figure 2-3. Images of 1 μm fluorescent microspheres at low magnification. Whole view field of an 80×80 μm before (left) and after (right) AO correction with parameters retrieved during optimization. [40]

In widefield microscopy with flood illumination of the sample area, aberration correction is typically applied only to the detection path because aberrations in the illumination path do not affect the quality of the image. Due to the broadband and randomly polarized nature of the detected light, DMs are primarily used in these applications [41], [42].

In general, in aberration correction with wavefront detection systems, fluorescent beads or fluorophore signals are usually used as guide stars to measure distorted wavefronts with wavefront detectors and then perform aberration compensation. For example, Azucena *et al.* [43] utilized fluorescent microspheres seeded in the Drosophila embryo as a benchmark employing a MEMS DM for aberration correction and a Shack-Hartmann wavefront sensor for wavefront detection. Their approach was able to improve the Strehl ratio by two times on average and as much as ten times when imaging through 100 μm of tissue. Reinig *et al.* [44] used a wavefront sensor and a DM to improve image quality, point spread function, and SNR when imaging the cortex of YFP-H mice. When imaging fine neuronal processes and subcellular dynamics within the zebrafish brain, Wang *et al.* [45] demonstrated adaptive correction of complex optical aberrations using a descanned, laser-induced

guide star and direct wavefront sensing. Diffraction-limited imaging was recovered over large volumes (>240 mm per side).

Sensorless aberration correction techniques include coherent optical adaptive techniques, genetic algorithms, and hill-climbing algorithms. As a result, they improve image brightness, SNR, and resolution. Ji *et al.* [46], for example, used a sensorless adaptive two-photon microscope to restore the diffraction-limited resolution in the mouse cortex at 450 μm depth. In their work, researchers improved the axial resolution by three-folds and increased the signal from small neuronal structures by five-folds.

Adaptive optics with wavefront detection significantly differs from that without wavefront detection. While the first method provides high accuracy and speed, it also requires a complex optics system and is more expensive. In addition, fluorescence guide stars involve complex biological processes and may harm the sample. Although adaptive optics without wavefront detection is a simple method and low cost, it has one drawback. Numerous iterative calculations make this type of aberration correction system time-consuming. In addition, this method can lead to photobleaching of fluorescent samples, which can hinder imaging [47].

2.2 Axial scanning applications

Axial scanning plays a significant role in many applications of endomicroscopy, confocal microscopy, and other microscopy types. Axial scanning enables the acquisition of high-resolution three-dimensional images of various biological structures and mechanisms. For example, observing and understanding dynamic biological phenomena such as drug delivery, polarity, environmental relaxation, and electrostatic potentials in cell membranes is imperative. In most imaging modalities, the xy planes are acquired at different depths and then combined using a reconstruction algorithm to create a three-dimensional image. Usually, a stage or imaging optics are physically moved to change the location of a focal plane using motors or linear actuators [48]. The disadvantages to this method are

slow mechanical scanning rates, vibrations, and artifacts introduced during live imaging, as well as the bulky and expensive nature of the system [49]. An optical approach to shifting the focus is an alternative method to solve these problems.

Optical axial scanning can be achieved by introducing a stationary active element called a varifocal element. Prime examples of varifocal elements include liquid-filled lenses, liquid crystals (LCs), vertical microlens scanners, and DMs [48]. Most achieve the focal shift by changing their optical and/or geometric properties.

An LC is a thermodynamically stable phase with properties between a liquid and a solid crystal. The refractive index of LC lenses can be altered by applying an electrostatic field and changing the orientation of nematic molecules. This technique can be used to control the focal plane location in axial scanning. Low power consumption and thin thickness are the two main advantages of LC lenses. In addition, LCs can control aberration with fine precision, and their step response is usually more than 300 ms [48]. Lin *et al.* [50] categorized LC lenses into four different groups: 1) GRIN LC lenses with a homogeneous cell gap, 2) Non-GRIN LC lenses with an inhomogeneous cell gap, 3) Diffractive LC lenses, and 4) LC lenses controlled by polarization. A liquid crystal device made of eight annular zones was designed and constructed by Solodar *et al.* [51]. Using this 4 mm diameter device as an SLM allowed them to shape beams and extend the depth of field. At 632 nm wavelength, the focal length of the LC lens ranged from 2485 mm to 16165 mm. In another work done by Bagramyan *et al.* [52], fixed gradient index and electrically tunable liquid crystal lenses (TLCLs) were utilized for adaptive 3D microendoscopy. TLCLs' properties were controlled by changing the frequency and keeping the voltage constant, resulting in a focal shift of 74±3 μm. The system was successfully tested *in-vivo* for mouse brain imaging at different depths, as shown in Figure 2-4. In other studies, two dielectric lenses were used to control how the electric field orients the LCs, increasing the control over wavefront shapes [53], [54].

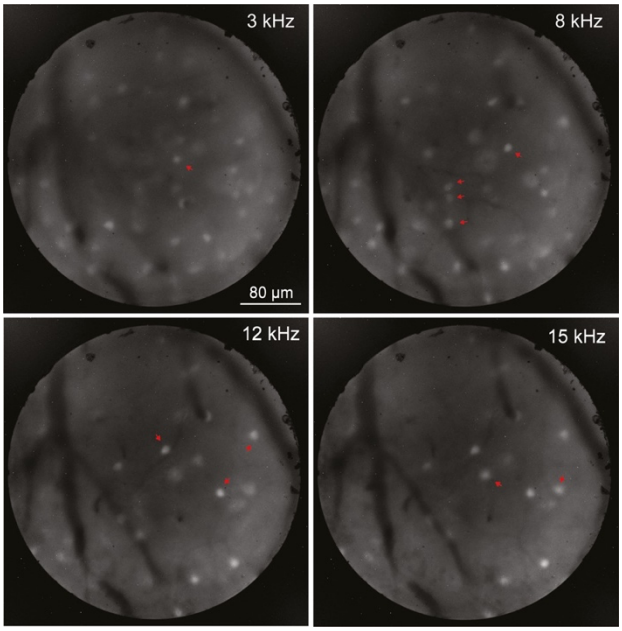

Figure 2-4. Motion-free variable-depth in-vivo imaging of interneurons in the adult mouse cortex. Defining 3 kHz as the starting position, the spatial shifts for 8 kHz, 12 kHz, and 15 kHz were 31 ± 1 µm, 56 ± 2 µm, and 69 ± 3 µm, respectively. [52]

Liquid-filled lenses are very cost-effective, but their fine shape control is usually limited [48]. They come in a variety of types, including but not limited to pneumatic, electromagnetic, electrochemical, hydrogel, electrowetting, and dielectrophoresis [55]. There are two ways to tune micro-optofluidic lenses: refractive index or geometry [56]. Tehrani *et al.* [57] used liquid-filled lenses to provide fast axial scanning for two-photon microscopy and applied it to imaging tissue-cleared mouse brain slices.

According to Doblas *et al.* [58], the liquid lens (LL) should be integrated at the aperture stop of telecentric microscopes. By tuning the focal length of LL and scanning the specimen axially, 3D images are acquired. Neither the resolution nor the magnification of the imaging system is affected by this method, according to the authors. Additionally, they claim that the suggested technique works with any commercial optical microscope [58]. One creative way to actuate liquid-filled microlenses is by using stimuli-responsive hydrogels, as reported by Dong *et al* [59]. The microlenses were no more than

500 μm in diameter. The researchers were able to obtain focal lengths varying from ∞ to −∞. However, their response times ranged from 10 to 30 s.

Finally, deformable mirrors are the most common varifocal devices. As mentioned earlier, they have fast step response, achromatic performance, excellent control over surface shape, and they are cost-effective and easy to manufacture. Peinado *et al.* [60] utilised a continuous DM for wavefront shaping and consequently scanning axially over the specimen. The adaptive system produced comparable results to those obtained using a conventional linear stage that moved the objective mechanically. Another example is the successful use of DM in adaptive optics scanning laser ophthalmoscope (AOSLO) setup for optical sectioning of the retinal layers [61]. First, during imaging, this AOSLO is focused on the external limiting membrane with the mosaic of cone photoreceptors. Then, imaging of the inner retina with visible blood vessels can be obtained using the DM to change the focal plane's location. Finally, the focus can be moved to the retina surface, allowing for observation of the striation of the nerve fiber bundles.

In conclusion, each varifocal device has its advantages and disadvantages. In choosing a varifocal device, one should carefully consider the study's purpose, desired outcomes, and affordability. More advanced devices will be developed with time, and the development of tools, increased knowledge leading to dynamic three-dimensional high-resolution imaging of biological specimens.

Chapter 3: Deformable mirror-based photoacoustic remote sensing (PARS) microscopy for depth scanning

Notes of acknowledgement

This chapter describes a study demonstrating the first use of a deformable mirror-based PARS microscopy with a depth scanning capability for label-free, non-contact, in-vivo imaging of chicken embryo chorioallantoic membrane (CAM) vasculature. It is based on the following journal manuscript (currently in review):

Lyazzat Mukhangaliyeva, Samed Kocer, Alkris Warren, Kevan Bell, Marian Boktor, Mustafa Yavuz, Eihab Abdel-Rahman, and Parsin Haji Reza, "Deformable mirror-based photoacoustic remote sensing (PARS) microscopy for depth scanning" submitted on August 1st, 2022 to Biomedical Optics Express.

Author contributions

Lyazzat Mukhangaliyeva designed the deformable mirror-based PARS system suitable for depth scanning, prepared and ordered the optical and digital components of the system, constructed the PARS system, conducted the experiments, processed the images, interpreted the data, prepared the figures, and wrote the main manuscript.

Samed Kocer characterized, set up and operated the deformable mirror, helped with constructing the PARS system, conducting experiments, and interpreting results.

Alkris Warren helped with designing and building the PARS system and interpreting the results.

Kevan Bell helped with designing and building the PARS system and interpreting the results.

Marian Boktor helped with image processing and preparing the figures.

Mustafa Yavuz contributed to the characterization of DM and the interpretation of its results.

Eihab Abdel-Rahman conceived the study, contributed to the interpretation of all results, and acted as the co-primary investigator.

Parsin Haji Reza conceived the study, contributed to the interpretation of all results, and acted as the co-primary investigator.

All authors contributed to the final version for publication.

3.1 Introduction

As was discussed in Chapter 1, conventional PARS microscopy architectures have been optimized primarily to acquire two-dimensional data. Volumetric imaging is achieved by mechanical scanning. An optical approach to shifting the focus may enable PARS to image larger volumes at higher speeds and at high resolution for multiple applications, including brain imaging [62], tumor angiogenesis [63][64], and oxygen saturation studies [19].

In this work, a DM was integrated into a PARS microscope for microvasculature imaging at varying depths. The DM utilized in experiments is a novel continuous MEMS DM [65]. It features a simplified control mechanism and a resonant electrostatic actuation scheme that employs a single harmonic drive signal to replicate up to 8 low and high-order Zernike modes. This actuation methodology eliminates the need for individually addressable electrodes, complex control mechanisms, and associated hardware. Furthermore, the DM's stroke is increased by dynamic amplification, which occurs when the DM is driven at resonance [66].

In the experiments, the characteristics of the DM were used to create an optical model and predict the focal shift using Zemax. Then, the focus shifting ability of the DM was characterized experimentally by utilizing a 532-nm scattering microscope embedded in a PARS microscope. Subsequently, the axial scanning capabilities of DM-based PARS microscopy were demonstrated by imaging carbon fibers. Finally, in-vivo PARS imaging of blood vessels in chicken chorioallantoic membrane (CAM) models were performed at different depths by optically shifting the focal plane.

3.2 Methods

3.2.1 Resonant deformable mirror structure and operation

The MEMS DM [65] used in the experiments is made of a 1.6 mm diameter crystal silicon plate with a thickness of 10 μm, Figure 3-1A, covered with a 75 nm thick gold layer to create a reflective

surface. Eight equally spaced beams support the mirror plate. Electrostatic actuation drives the DM via 49 electrodes patterned in four concentric tiers on the bottom wafer 20 μm below the mirror plate. Figure 3-1B shows two DMs on a chip carrier. One of them is wire-bonded and used in the experiment. The electric field is created by applying a single resonant harmonic voltage to one or more electrodes while the mirror plate is grounded. The operating principle of the DM depends on the use of a pulsed laser beam. The pulse repetition rate (PRR) of the laser is synchronized with the DM oscillations.

The resonant DM can produce the eight lowest order Zernike modes, namely defocus, primary coma, astigmatism, primary spherical, trefoil, tetrafoil, secondary coma, and secondary spherical at different excitation frequencies and a single excitation signal. For example, the mirror is actuated at 8 kHz for a defocus mode and 40.5 kHz for a primary spherical mode. This study used the defocus mode, the first axisymmetric mode of the DM shown in Figure 3-1C, as a varifocal mirror for axial scanning. The mirror was actuated by applying a harmonic voltage waveform with an amplitude of 150 V and a frequency of 8 kHz to all actuation electrodes. Its radius of curvature was controlled by varying the phase angle ϕ between the pulse signal of the incident laser beam and the drive signal of the DM.

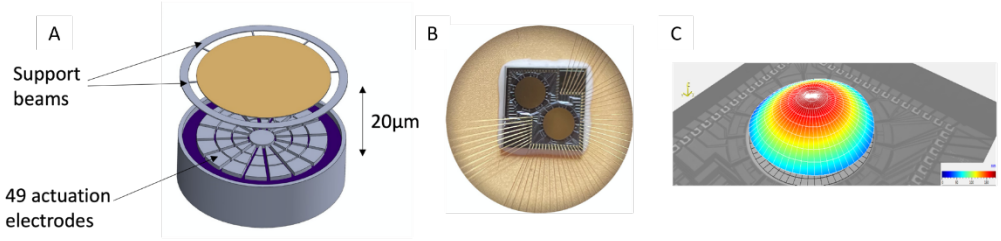

Figure 3-1. Novel MEMS DM utilized for depth scanning.
A. The DM structure. B. Corresponding light photograph, C. Defocus mode obtained using a Laser Doppler Vibrometer. [65], [66]

3.2.2 PARS system architecture

The PARS system illustrated in Figure 3-2 is a modified version of the traditional PARS imaging setup outlined in [16]. The 532-nm 1.5 ns output of the fiber laser (GLPM-10, IPG Photonics)

served as an excitation source for the imaging system. The output beam of the laser was coupled to an optical fiber (PM-460-HP, Thorlabs). The fiber output was coupled to a collimator mounted on a rotating holder to control the polarization. The beam size was reduced to ~750 μm using a 5X Galilean beam condenser (BC) to effectively utilize the defocus mode of the DM. A polarizing beam splitter (PBS) transmitted ~90% of the excitation light to the DM. The DM was adjusted to be orthogonal to the incident beam. The reflected light from the DM was diverted towards a collimating lens (L) through the same PBS. The location of the collimating lens was determined using Zemax simulation, and a detailed description is provided in Section 2.3. The detection light was delivered by an 830-nm superluminescent diode (SLD830S-A20, Thorlabs). The excitation and detection beams were combined using a dichroic mirror (DMSP605R) and directed toward the objective lens using a large-beam galvanometer scanning mirror (GVS012/M, Thorlabs). The two beams were co-focused onto the sample using a 20X 0.4 numerical aperture (NA) objective (MY20X-824, Thorlabs). The detection light reflected from the specimen was collected by the same objective and guided onto an avalanche photodiode (APD430A/M, Thorlabs). An additional photodiode (DET10A2, Thorlabs), PBS, and a QWP were incorporated into the excitation path to collect the back-scattered excitation light from the sample by implementing a 532-nm scattering microscope. The 532 nm scattering microscope provided information on the location of the excitation plane, allowing better alignment of the system. In Figure 3-2, blue dashed lines illustrate wavefront control provided by the deformable mirror, while pink dashed lines demonstrate axial scanning. A point acquisition was acquired for each pixel and recorded by a high-speed digitizer connected to the two photodiodes in the system. All signal processing and image formation steps were performed in C/C++ and MATLAB environments.

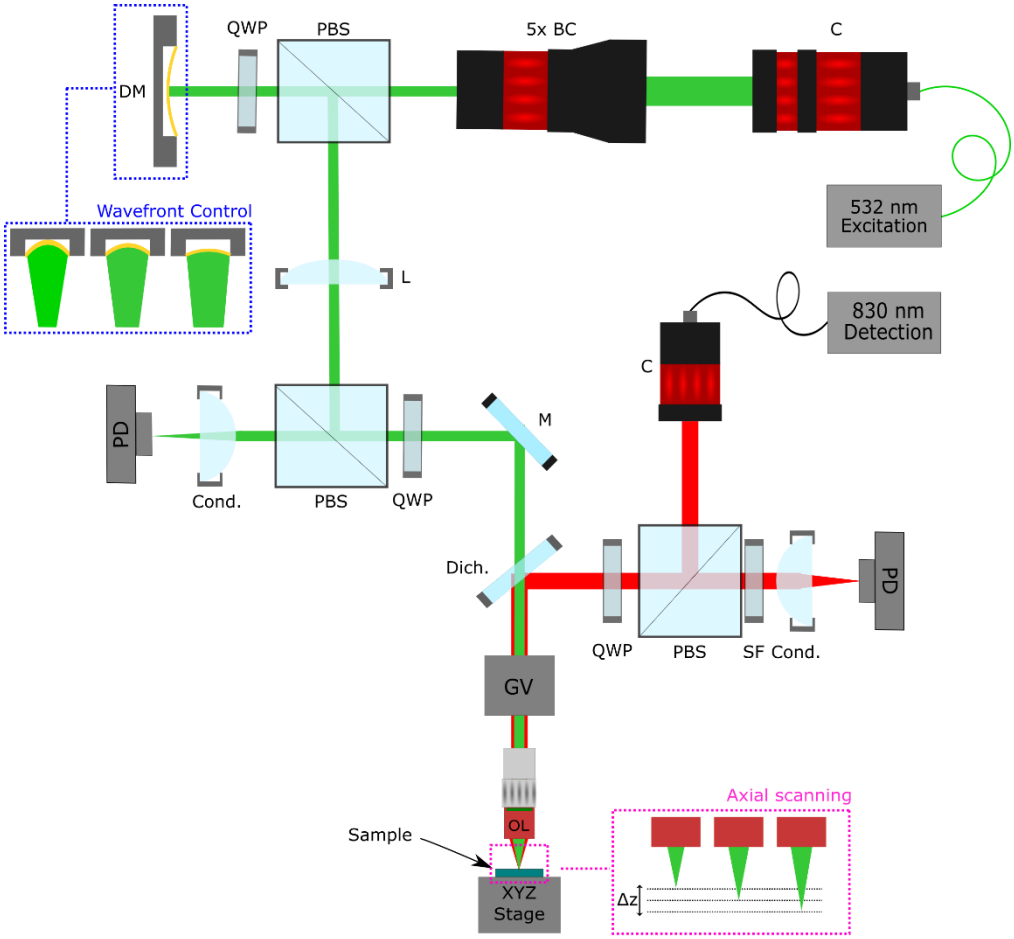

Figure 3-2. Simplified PARS optical setup.
C: collimator, BC: beam condenser, PBS: polarized beam splitter, QWP: quarter-wave plate, DM: deformable mirror, L: collimating lens, Cond: condenser lens, M: mirror, Dich. M: dichroic mirror, SF: spectral filter, GV: galvanometer, OL: objective lens.

3.2.3 Zemax optical model

Zemax was used to simulate an optical setup. A 532 nm collimated input beam of 750 µm was used to represent an ideally collimated incoming beam illuminating the DM, as shown in Figure 3-3. The wavelength was set to 532 nm as the DM was only incorporated on the excitation path in the PARS system. The DM was represented by a standard surface type with a clear semi-diameter of 800 µm. The radii of curvatures of the DM varied from 220 mm to 380 mm based on previous experimental results [65] with a step size of 10 mm. The incoming light first passed through a PBS. A positive lens

(LA1708-AB, Thorlabs) was used as a collimating lens. The location of the collimating lens was determined by fixing the radius of curvature of the DM at 350 mm and optimizing it to obtain the collimated beam out. Finally, the last element in the setup was a paraxial lens with a focal length of 10 mm used to focus the light. The distance between the PBS and the DM was based on the physical setup of the PARS system. The location of the focal plane corresponded to the distance (thickness in Zemax) after the paraxial lens was calculated using the thickness solve – marginal ray height.

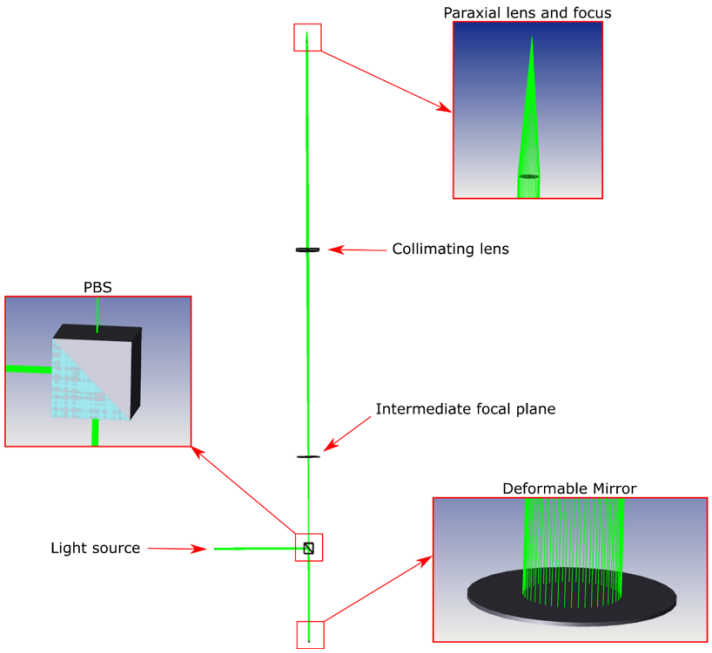

Figure 3-3. Optical design in Zemax.

3.2.4 Chicken chorioallantoic membrane (CAM) model preparation

CAM models were prepared in-house as cost-effective and easy-to-handle samples for in-vivo imaging of blood vessels and microvasculature. For that purpose, fertilized eggs from the White Leghorn breed were purchased from Frey's Hatchery in St. Jacobs, ON, Canada. The fertilized eggs were then placed into the automatic rotating hatcher for 72 hours at 37°C and relative humidity of 65-70%. After 72 hours, the eggs were placed on their sides for a resting period of 60 minutes to allow the embryo to rise to the top of the egg. Meanwhile, a CAM container was prepared by placing a plastic

film on the top of a plastic cup and pushed down to form a trough. The plastic film was secured with a rubber band following the protocol outlined by Naik *et al.* [67]. The plastic film was then sprayed with 70% Isopropyl Alcohol (IPA) before the cracked eggs were dropped into their respective CAM holders. A Dremel handheld saw attached to a vertical stand was used to drill into the surface of the eggshells with a circular cutting disc. Before drilling each egg, the disc and eggshells were sprayed and disinfected with 70% IPA. The eggs were then held sideways above the Dremel disc while maintaining the orientation achieved during the resting process. A long but shallow cut was made at the surface of the eggshell from the 90-degree mark to the 270-degree mark, keeping the yolk at the top and avoiding any rotational movements. Once the shallow cut was completed, the egg was placed down on the plastic film within the CAM holder and gently cracked by pressing it against the sides of the CAM holder. After the extraction process was complete, the ex-ovo CAM was covered with a perforated plastic film for ventilation and maintenance of proper humidity. The ex-ovo CAMs were then placed inside a plastic container holding 2 inches of warm water. The plastic containers with the ex-ovo CAMs were then placed in the incubator at 37.8°C and with a relative humidity of >68% up to the imaging day. Figure 3-4 represents the ex-ovo CAM development from day 0 through day 12. This study used 9 to 12-days-old CAMs for blood vessel imaging.

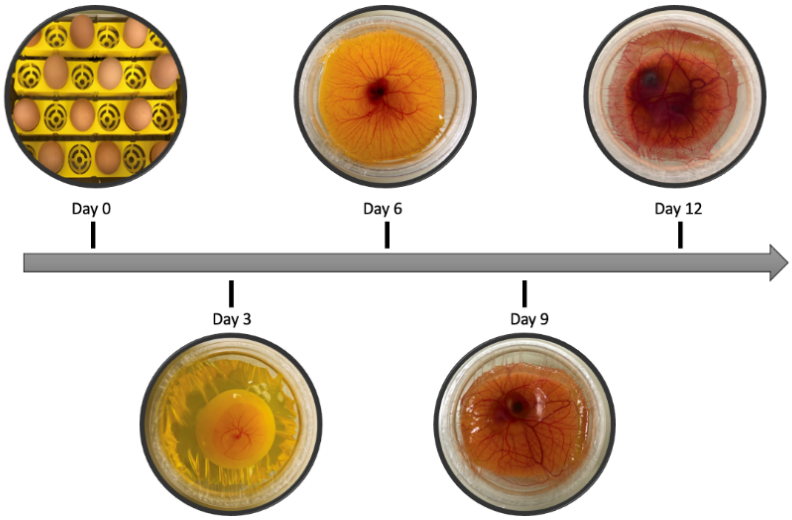

Figure 3-4. Ex-ovo CAM development from day 0 through day 12

3.3 Results

3.3.1 Optical and experimental axial scanning capability

As a first step, the axial scanning capability of the DM was approximated in Zemax. The distance between the focusing lens and the focal plane location was calculated by varying the radius of curvature of the DM. The focal length of the focusing lens is equal to 10 mm. When an incoming beam is perfectly collimated, the distance between the focusing lens and the location of the focal plane is, therefore, equal to 10 mm. As the curvature of the DM changed from 220 mm to 380 mm, the distance between the focusing lens and the location of the focal plane from 9.84 mm to 10.04 mm, as shown in Table 3-1. As a result, the total focal shift calculated by the Zemax simulation was 200 μm.

Table 3-1. The focal plane distances from the paraxial lens for different radii of curvatures

Radius of curvature (mm)	**220**	**240**	**260**	**280**	**300**	**320**	**340**	**360**	**380**
Focal plane location (mm)	9.84	9.86	9.89	9.91	9.94	9.96	9.99	10.01	10.04

The focal shifting ability of the DM was validated experimentally by imaging a 1951 United States Air Force (USAF) resolution target. The images were acquired using a 532-nm scattering

microscope setup. Figure 3-5A shows images of a 1951 USAF resolution target from group 3, elements 5 and 6. The smallest element (group 3 element 6) has a resolution of 14.30 lp/mm, corresponding to a line spacing of ~70 μm. The images were obtained at three different depths by moving the XYZ stage from 0 μm to 120 μm and 240 μm. The DM surface was deformed at each depth by varying the driving phase angle from 0° to 45° and 90°. The total number of images acquired was 9. Higher resolution images highlighted in black were obtained when the sample plane and the focal plane coincided. The edge spread function (ESF) was acquired along the black line for each image. The line spread function (LSF), the derivative of ESF, was plotted, and the full-width half maximum (FWHM) values were calculated to obtain image resolution, as illustrated in Figure 3-5B. Figure 3-5C demonstrates that at a depth of 0 μm, the FWHM increased from 4.5 μm to 11.7 μm as the phase angle changed from 0° to 45° to 90°, and the image resolution decreased, consequently. At a depth of 120 μm, the most resolved image was in the middle and had an FWHM value of 5 μm. Lastly, at a depth of 240 μm, the FWHM decreased from 10.22 μm to 4.47 μm, as the phase angle increased from 0° to 90°, respectively. The experimental results suggest that the total focal shift provided by the DM is 240 μm.

It may be noted that the Zemax simulation and the experimental results differ by 40 μm of focal shift. This might result from using a paraxial lens in Zemax and an actual objective lens in the experiments. Ideally, a black box of the objective lens would be used instead of the paraxial lens to improve the simulation results. In addition, Zemax's simulation used an ideally collimated beam, which rarely exists in reality. Moreover, while the distances between the optical components in Zemax are based on the experimental setup, they are not 100% precise. Lastly, the radii of curvature used in the Zemax optical design were obtained at 200 V, while the focal shifting experiments on the USAF targets

were performed at 300 V of the actuation voltage. All the factors mentioned above need to be addressed for the simulation results to better match the experimental results.

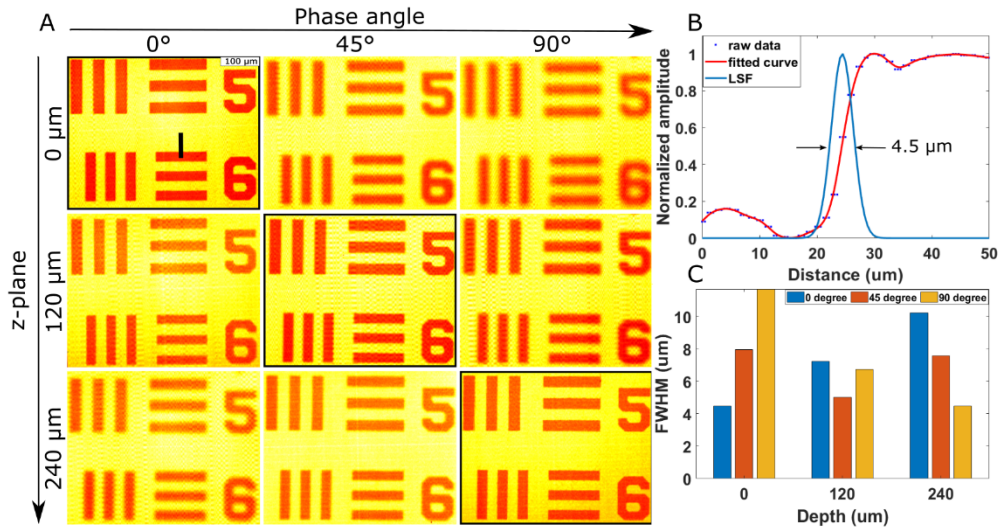

Figure 3-5. Demonstration of focus shifting ability of the system on USAF resolution targets. A. USAF resolution target imaging with a 532-nm scattering microscope. B. The edge spread function (ESF) and line spread function (LSF) from raw data. C. Full-width half maximum (FWHM) values at different depths.

3.3.2 Phantom imaging with PARS

Next, the DM-based PARS system's ability to optically shift the focal plane was demonstrated on carbon fibers. The imaging setup shown in Figure 3-6A is composed of placing a layer of carbon fibers on a glass slide, covering it with a cover glass, and then adding another layer of carbon fibers on top. As a result, two layers of carbon fibers arranged perpendicular to each other and separated by a cover glass are obtained. The thickness of the cover glass was measured to be 151 µm. The image of the top layer of carbon fibers was acquired at a 0° phase angle, Figure 3-6B. A further increase in phase angle to 60° allowed an image of the carbon fibers at the bottom layer to be obtained as the focal plane moved deeper into the sample, Figure 3-6C. Meanwhile, the mechanical stage remained stationary within the system. Shadows cast by the top layer of carbon fibers can be seen in Figure 3-6C, as indicated by white arrows. In Figure 3-6D, the top (green) and bottom layers (purple) of carbon fibers

were reconstructed to create a single image with depth information. As demonstrated by the experiment, we were able to optically shift the focal plane to image two layers of carbon fibers separated by a 151 μm thick cover glass using the DM for wavefront control within the PARS microscope.

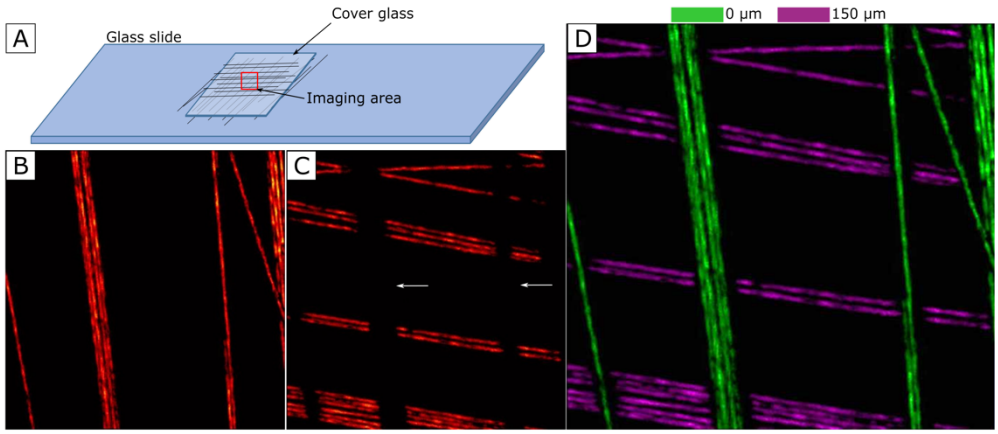

Figure 3-6. Phantom imaging of carbon fibers with PARS system.
A. Sample setup for imaging. B. Top layer carbon fibers imaged at 0 μm depth. C. Bottom layer carbon fibers imaged at 150 μm depth. White arrows indicate the shadow cast by the top layer of carbon fibers. D. Overlayed images of carbon fibers at different depths.

3.3.3 DM based photoacoustic microscopy in in-vivo studies

To demonstrate the in-vivo capabilities of the system, the blood vasculature of CAMs was imaged, as shown in Figure 3-7. The CAM models were placed in an ice bath during the imaging session to reduce motion artifacts. Images were acquired with 16 kHz pulse repetition rates of the excitation laser. As the z-location of the focal plane increased with the increasing phase angle, the PARS microscope imaged blood vessels at deeper layers. At 0 μm, there were almost no blood vessels observed, except for a slight hint that can be seen in the lower part of the image indicated by white arrows. As the focal plane moved approximately 13 μm deeper into the sample, a blood vessel was imaged, and some capillary beds were captured, but the microscope's resolution was not enough to resolve them. It can also be noticed that the blood vessel was not ideally located on the imaging plane and its left side went deeper into the sample. By moving another 13 μm deeper into the sample, the whole blood vessel can be seen. At approximately 90 μm, the intensity decreased as the focus moved

beyond the blood vessel. However, the blood vessels can still be observed at that depth, as the biomolecules still absorb the excitation light even when not at an ideal focal plane.

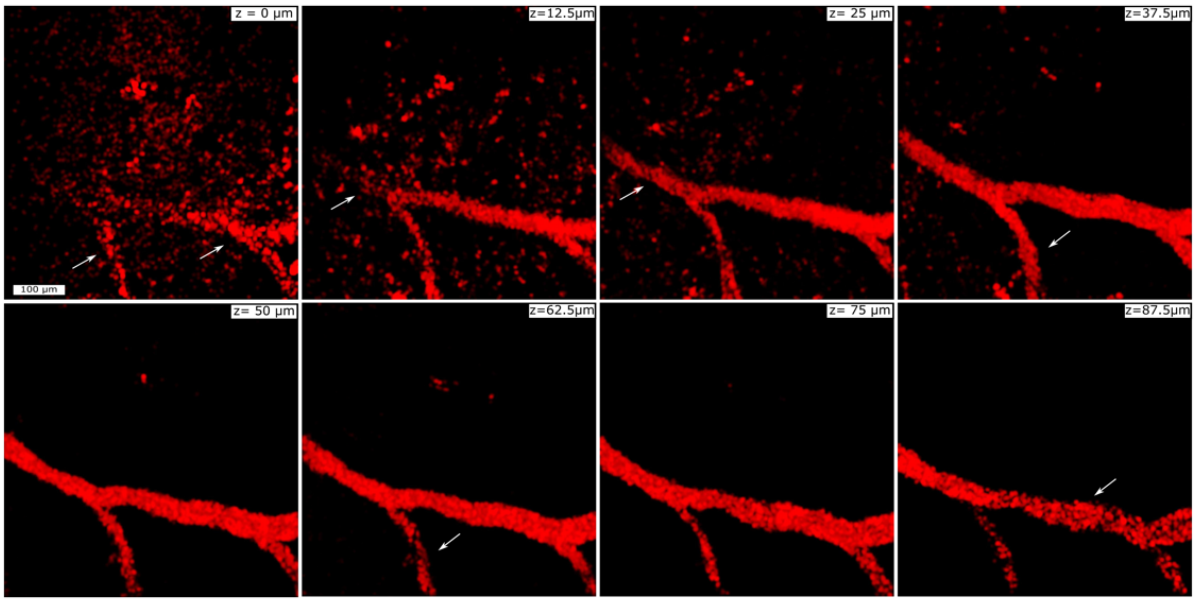

Figure 3-7. In-vivo imaging of CAM models at different depths using PARS microscopy with DM. FOV is 660x660 µm^2

In this work, we have demonstrated the ability of the PARS system to optically shift the focal plane using the DM on carbon fibers and CAM blood vasculature. The technology opens the door to developing non-contact, label-free, and aberration-free optical systems with axial scanning capabilities for rapid, high-resolution volumetric imaging of biological tissues. For instance, an ideal high-resolution DM-based PARS system with rapid depth scanning capability would be able to image newly formed vessels deep within tumors that tend to be very small and exhibit very low signals in angiogenesis studies.

Future work will focus on improving the speed of the DM-based PARS system to provide rapid depth scanning by automating the phase angle change. The resolution of the system will also be enhanced by increasing the beam diameter and utilizing the full aperture of the objective lens. This will allow the system to visualize small structures such as capillary beds and red blood cells. Moreover, the

ability to optically shift the focal plane will be used for correcting chromatic shift caused by wavelength changes in multiwavelength applications such as oxygen saturation studies. Other modes of the deformable mirror can be used for aberration correction applications in PARS. For example, the primary spherical mode of the DM can be used to correct spherical aberrations in ophthalmology applications.

3.4 Conclusions

For many applications, such as brain imaging, tumor angiogenesis, or multiwavelength studies, shifting the focal plane optically, rather than mechanically, may be a more suitable method for imaging large volumes at high speeds and with high resolution. This work demonstrates the integration of a DM with PARS microscopy to enable optical depth scanning. The defocus mode of a novel DM was used as a varifocal mirror to shift the focal plane. The focal shifting ability of the DM was first simulated in Zemax and then demonstrated experimentally on USAF targets. The results suggest that 240 μm of optical focal shift can be achieved, experimentally. The depth scanning ability of the PARS system was then demonstrated on carbon fibers. Two layers of carbon fibers separated by a 151 μm cover glass were imaged by optically moving the focal plane from the top layer to the bottom layer. Finally, the DM-based PARS microscope's axial scanning capability was validated in in-vivo imaging of blood vessels in chicken CAM models.

Chapter 4: Wide-field photoacoustic remote sensing (PARS) microscopy

Notes of acknowledgement

This chapter summarizes results from a study that showed the first use of a scan lens in PARS microscopy for wide field of view (WFOV) imaging. The content of this chapter is intended to be submitted to a scientific journal.

Author contributions

Lyazzat Mukhangaliyeva designed the scan lens-based WFOV PARS system, prepared and ordered the optical and digital components of the system, constructed the PARS system, conducted the experiments, processed the images, interpreted the data, prepared the figures, and wrote the first draft of the paper.

Alkris Warren helped with designing and building the WFOV-PARS system and interpreting the results.

Marian Boktor helped with image processing and preparing the figures.

Parsin Haji Reza conceived the study, contributed to the interpretation of all results, and acted as the primary investigator.

All authors will contribute to the final version for publication.

4.1 Introduction

The advancement of scientific knowledge and tools has enabled researchers to observe and study things previously unthinkable. Optical microscopes allow the observer to see biological specimens and physiological processes that may not be visible to the naked eye. However, most optical microscopes still have a trade-off between the field of view, resolution, and imaging speed. The common method for obtaining large FOV imaging is mechanically scanning small areas laterally at different positions and stitching them together. However, mechanical scanning is slow and can cause sample agitation and motion artifacts. For example, Recher *et al.* [68] investigated how mechanical scanning negatively affects sensitive samples. The experiment involved cells encapsulated in a porous alginate shell. Their geometry requires suspending the samples in a culture medium while avoiding agitation. A mechanical stage was used to move the samples 500 µm to the left during the experiment and then return them to their original position. This process caused cell capsules to rotate, Figure 4-1. Since each capsule was affected differently, post-processing cannot correct the problem, so mechanical scanning is not an option for long-term imaging and tracking sensitive samples.

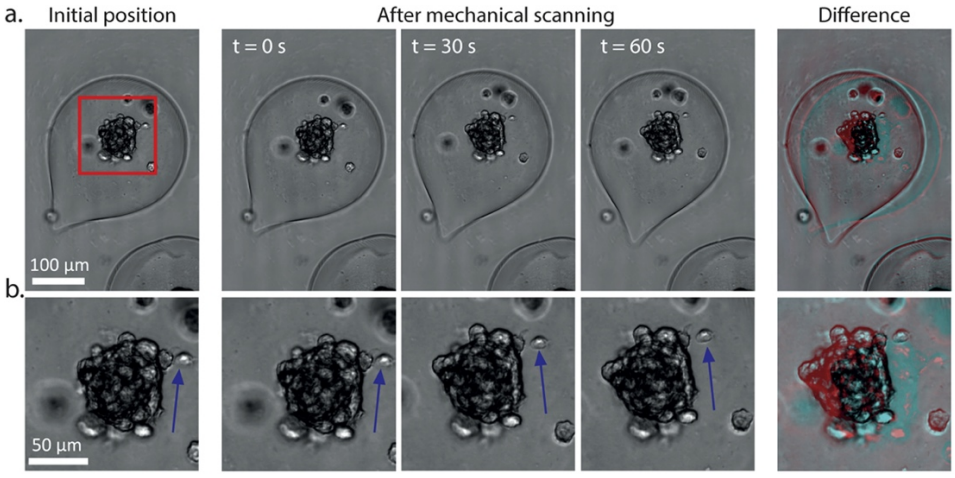

Figure 4-1. Effect of mechanical scanning when imaging capsules with wide-field microscopy. (a) The sample is mechanically scanned to the left with a motorized stage. (b) Zoom in of the area corresponding to the red square in (a). [68]

Moreover, mechanical scanning is not suitable for imaging fast dynamic environments due to its slow acquisition speeds. Combining lateral optical scanning with mechanical repositioning can improve the process, but some applications will still require a faster system. Potsaid *et al.* named several common ways to achieve wide-field imaging [69], including using multiple parfocal objectives, designing a zoom lens, moving a microscope, or using multiple microscopes. Depending on the method, there are advantages and disadvantages in terms of the resolution, speed, agitation of the sample, manufacturability, and versatility. Generally, as resolution and imaging speed increase, these microscopes become more expensive and more difficult to reconfigure. Similarly, PARS microscopy utilizes mechanical scanning to obtain wide-field imaging. WFOV is usually achieved by mosaicking – aligning multiple small FOV images to construct one wide FOV image. For example, this method was effectively used to obtain a large field of view image of blood vessels [23] in an 8-week-old nude mouse's ear, as shown in Figure 4-2.

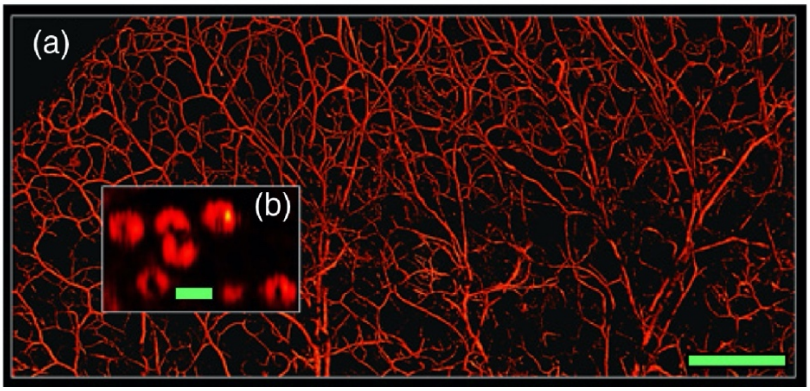

Figure 4-2. PARS imaging of mouse ear vasculature in the ear of an 8-week-old nude mouse (a) Image of en face microvasculature using the high-resolution mode (scale bar: 500 µm) (b) *In-vivo* image of red blood cells in the mouse ear using the high-resolution mode (scale bar: 5 µm). [23]

However, as was discussed previously, mechanical stage scanning suffers from various drawbacks, such as slow scanning speeds, motion artifacts, and sample agitation. As a result, this technique may not be suitable for bulky specimens or samples suspended in medium or very fast

dynamic environments. One way to achieve fast widefield optical scanning is by using a scan lens as an objective lens. An imaging technique like this is intended for applications in which high-resolution imaging can be sacrificed in exchange for widefield imaging. Scan lenses are specialized lenses that provide a flat image plane with relatively constant spot sizes. Several laser imaging systems use scan lenses, such as multiphoton imaging, optical coherence tomography, and confocal laser scanning microscopy [70]–[72]. Scan lenses can be used alone or with tube lenses to create infinity-corrected optical systems. There are two types of scan lenses: F-theta lenses and telecentric lenses. The focal spot position in F-theta lenses depends on the product of the focal length (F) and the deflection angle (θ). These lenses are widely used in laser marking and display applications. On the other hand, telecentric lenses are designed to have a normal incidence beam over the entire target plane. These lenses also have minimal optical aberration, low F-theta distortion, and a large field of view. For example, Martell *et al.* [73] have integrated a telecentric scan lens to achieve a fast, widefield optical scan mode OCT. This system also features complimentary PARS microscopy that provides widefield *in-vivo* imaging of blood vasculature through mechanical scanning only.

Chapter 4 presents a feasibility study where a telecentric lens (SL50-CLS2, Thorlabs) was integrated with PARS microscopy to achieve fast WFOV optical scanning. The capability of the system is demonstrated on carbon fiber phantoms and chick embryo CAM vasculature.

4.2 Methods

4.2.1 WFOV-PARS system architecture

Figure 4-3 is the schematic of the WFOV-PARS system architecture. The excitation light is provided the fiber laser (GLPM-10, IPG Photonics) with the wavelength of 532 nm and a pulse width of 1.5 ns. The pulse repetition rate used for experiments varied from 50 kHz to 60 kHz. The output beam of the laser was coupled to an optical fiber (PM-460-HP, Thorlabs) and then collimated by a

zoom collimator (ZC618FC-A, Thorlabs) with the largest beam diameter of 3.5 mm. An 830-nm superluminescent diode (SLD830S-A20, Thorlabs) was used as the detection light source. The output detection beam diameter was 4 mm. A dichroic mirror (DMSP605R) was used to combine the excitation and detection beams. Large-beam galvanometer scanning mirror (GVS012/M, Thorlabs) was employed for lateral scanning. The excitation and detection beams were focused using a scan lens with an entrance pupil diameter of 4 mm. This scan lens is designed and optimized to work with laser scanning microscopy systems in the 450-1100 nm wavelength range. According to product specifications, this scan lens provides a maximum field of view of 14.1 x 14.1 mm^2. The same scan lens was used for collecting back-reflected detection light, which was guided to a photodiode. MATLAB and C/C++ were both used for signal processing and image formation.

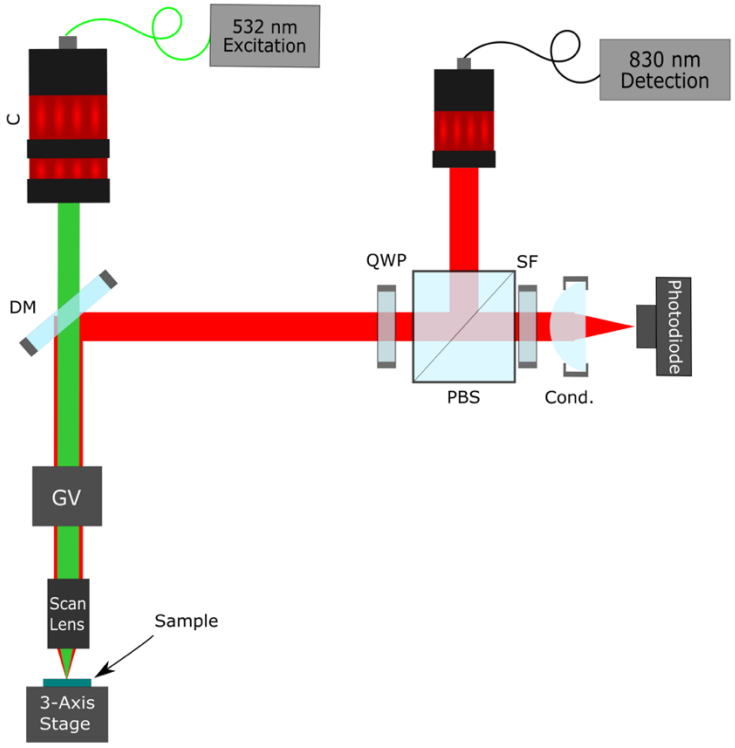

Figure 4-3. Simplified WFOV-PARS optical setup.
C: collimator, PBS: polarized beam splitter, QWP: quarter-wave plate, Cond: condenser lens, M: mirror, DM: dichroic mirror, SF: spectral filter, GV: galvanometer.

4.2.2 Sample preparation

The PARS system's WFOV scattering mode was evaluated with leaf vein skeletons as samples. Leaf vein skeletons were prepared in-house. On the day of the procedure, fresh, green, and preferably glossy leaves were obtained. Then, they were boiled for at least two hours in a pot with enough water to cover them and 1/2 cup of baking soda. To keep the process moving, water was constantly added. As soon as the boiling process was completed, the leaves were carefully transferred to a pot of cold water. With the help of a small and soft brush, the meaty parts of the leaves were washed off. Afterward, the leaf skeleton was carefully placed on a glass slide to dry. Figure 4-4 shows the light photograph of the leaf skeleton on the glass slides. Imaging the sample with the scattering microscope reveals the collenchyma cell walls that provide support to plant structures. The chick embryo CAM models used as biological tissue specimens for WFOV-PARS microscopy were prepared using the same protocol as outlined in Chapter 3, Section 3.2.4.

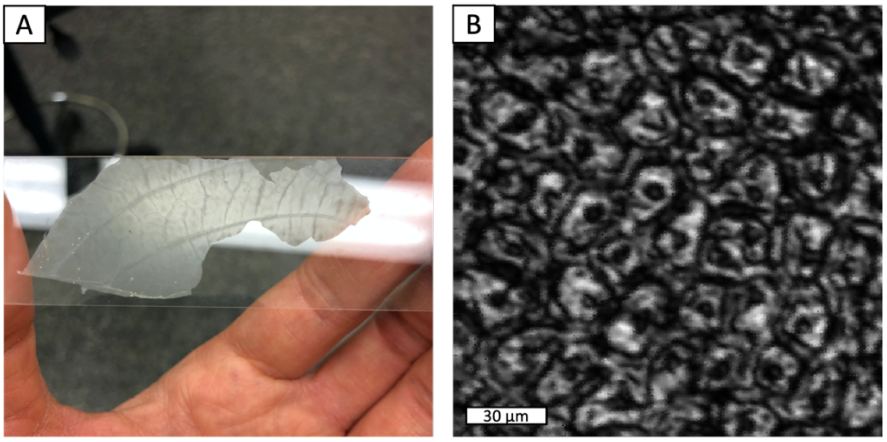

Figure 4-4. Leaf vein skeleton sample preparation.
A. Light photograph. B. Scattering image. FOV is 200×200 µm^2

4.3 Results and Discussion

4.3.1 System characterization

The beam diameter at focus (also known as a spot size) and depths of field for both excitation and detection beams were calculated using the two formulas below.

Spot size: $$2\omega_o = \frac{4M^2\lambda f}{\pi D} \quad (9)$$

Depth of field: $$DOF = 2z_R = 2\frac{\pi\omega_0^2}{M^2\lambda} \quad (10)$$

where λ is the wavelength of the light beam, f is the focal length of the lens, D is the beam diameter at lens, M^2 is the beam quality parameter (assuming M^2=1.2), ω_o is the beam waist, and z_R is the Rayleigh range of a Gaussian beam. The calculated results are presented in the

Table 4-1 below:

Table 4-1. Spot size and depth of field of excitation and detection beams.

Parameters	Excitation beam	Detection beam
Wavelength (nm)	532	830
Beam diameter at lens (mm)	3.4	4
Scan lens focal length (mm)	50	50
Beam quality M^2	1.2	1.2
Spot size (µm)	12	15.9
Depth of field (µm)	352	396

Based on the table, the theoretical depth of field is much worse than the theoretical lateral spot size. It is usually the case with most systems, but this is due to the very low NA of the scan lens - 0.04. To determine the actual lateral resolution of the system, we imaged group 3, elements 5 and 6 of the 1951 USAF resolution target with an FOV of 800×800 µm^2, Figure 4-5A. The image was acquired using only the 830 nm detection beam. The edge spread function (ESF, red line) was estimated by

fitting a curve to the raw data acquired along the dashed line, Figure 4-5B. To obtain the line spread function (LSF, blue line), we calculated the first derivative of the fitted ESF curve. According to the full width at half maximum (FWHM), the lateral resolution of the WFOV-PARS system was calculated to be 19.25 µm. The obtained lateral resolution is worse than the calculated theoretical spot size (15.9 µm) due to the possible aberrations coming from the misalignment of optics and the specimen.

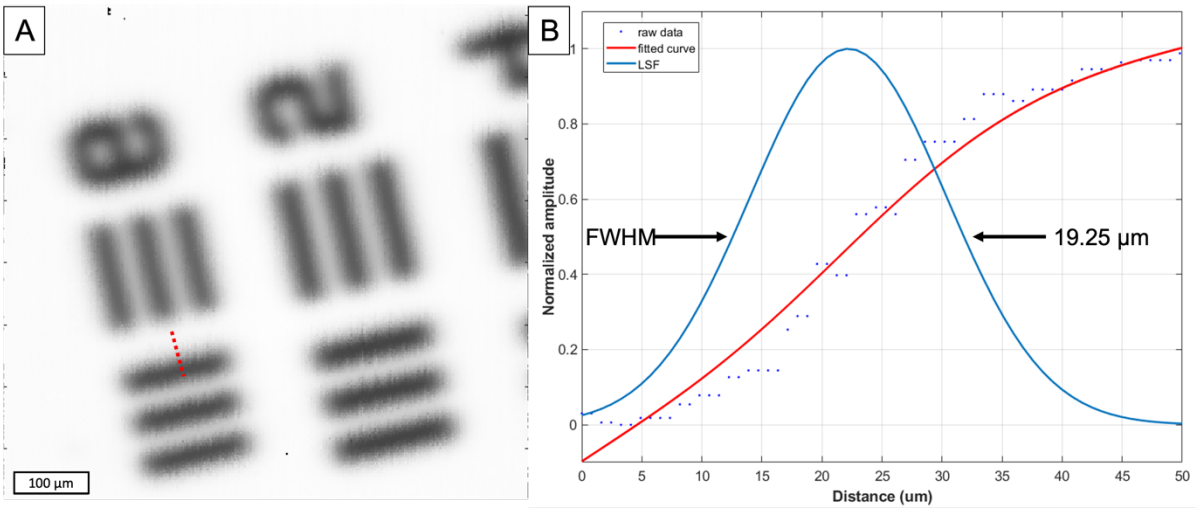

Figure 4-5. FWHM calculation of the USAF target element using 830 nm detection beam.

4.3.2 Phantom imaging experiments

We performed imaging experiments on leaf vein skeletons to verify the FOV of the scattering mode PARS system. For this purpose, only the detection path of the 830 nm light beam was enabled. 11.9×11.9 mm^2 large area of a leaf vein skeleton was imaged, as shown in Figure 4-6A. A smaller area 6.8×6.8 mm^2 was also obtained, Figure 4-6B. The detection power measured at the specimen was 3.7 mW. As can be clearly seen from the figures, although a large area was imaged with the scattering mode, the resolution is not enough to clearly resolve the veins or collenchyma cells.

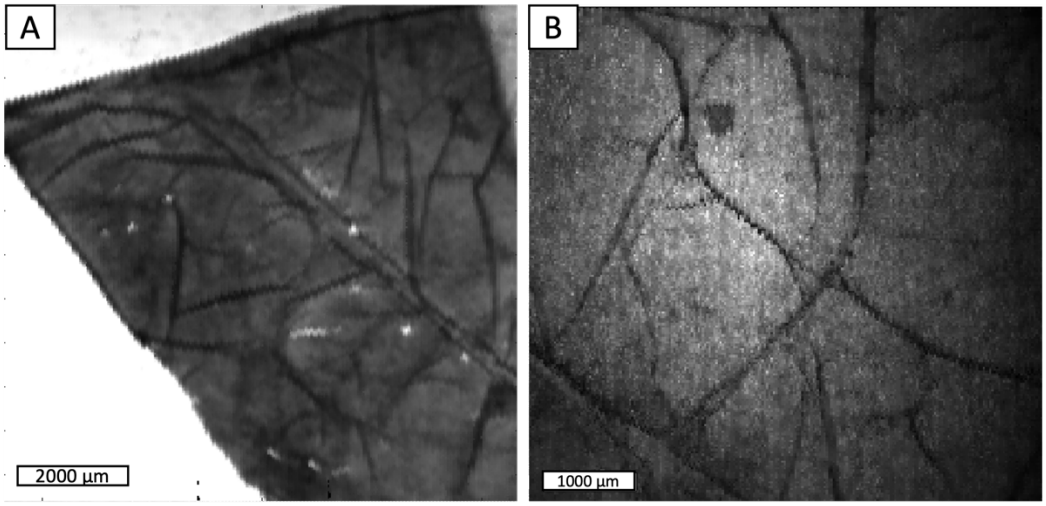

Figure 4-6. Leaf vein skeleton imaged with scattering microscope.
A. FOV is 11.9×11.9 mm² B. FOV is 6.8×6.8 mm²

As a next step, carbon fibers were used to test the WFOV-PARS system's performance. The image on the left, Figure 4-7A, has a FOV of 800×800 µm², whereas the image on the right, Figure 4-7B, has a FOV of 1600x1600 µm². Both images were obtained with approximately 25.5 mJ/cm² of fluence. Using the same procedure as discussed in Section 4.3.1, the FWHM along the dashed line was calculated to be 15.8 µm, as shown in Figure 4-7C. This measured FWHM value is also larger than the calculated theoretical spot size value for the excitation beam – 12 µm.

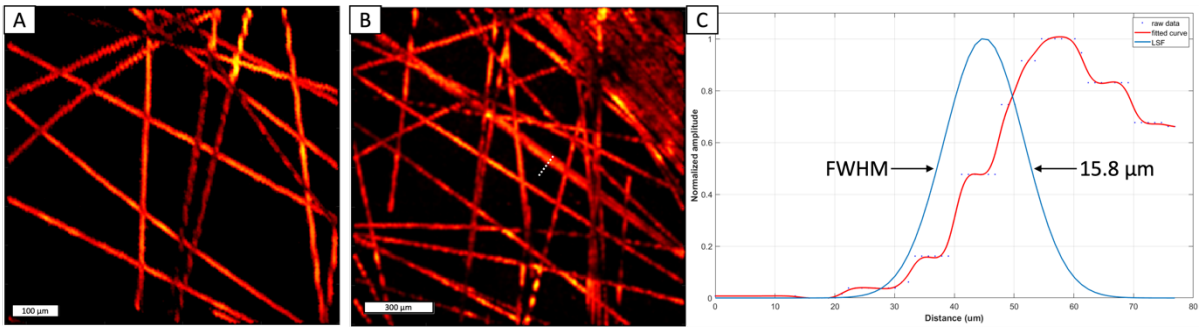

Figure 4-7. Carbon fiber network image acquired with a fixed gain balanced photodiode.
A. FOV is 800×800µm². B. FOV is 1600×1600µm². C. FWHM calculation along the white dashed line in B.

This system was improved through the replacement of a fixed gain balanced photodiode with a variable gain avalanche photodiode to increase its maximum responsivity from 0.53 A/W to 53 A/W. In subsequent experiments, we were able to obtain wider field of view images of carbon fibers. Figure 4-8A shows an image with a FOV of 6.8×6.8 mm^2, acquired with 90 mJ/cm^2 of fluence. The image on the right, Figure 4-8B, was obtained with lower fluence – 50 mJ/, and has a FOV of 8.5×8.5 mm^2.

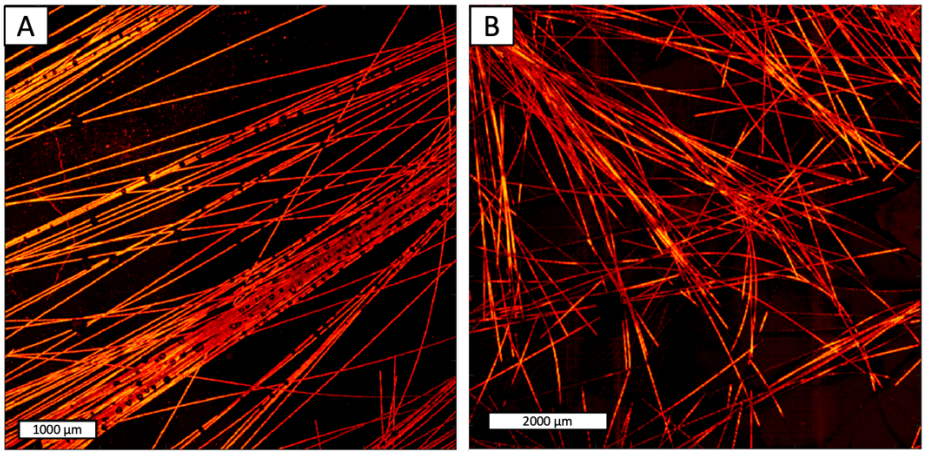

Figure 4-8. Carbon fiber network image acquired with a variable avalanche photodiode. A. FOV is 6.8×6.8 mm^2. B. FOV is 8.5×8.5 mm^2.

4.3.3 Biological tissue imaging experiments

To show the large-scale imaging capability of WFOV PARS, we carried out *in-vivo* imaging of the vascular network of the chicken embryo's CAM. Figure 4-9A presents a blood vessel imaged with a FOV of 1670×1670 μm^2. The blood vessel appears to have a very well-defined geometry, with diameters ranging from 40 µm to 80 µm. An overlay of the blood vessel image onto the scattering map is shown in Figure 4-9B. Both images were acquired during the same acquisition using the WFOV PARS microscopy. Scattering image provides additional information on the topography of the surrounding area of the blood vessel. Next, the FOV was increased to 3340×3340 μm^2 and the image of blood vessels *in-vivo* was obtained, as shown in Figure 4-9C. The resolution of the system decreased as we increased the FOV. Further, the depth of field increased, and the signals coming from capillaries

and blood vessels at various depths can be observed, but they cannot be resolved with the current system setup.

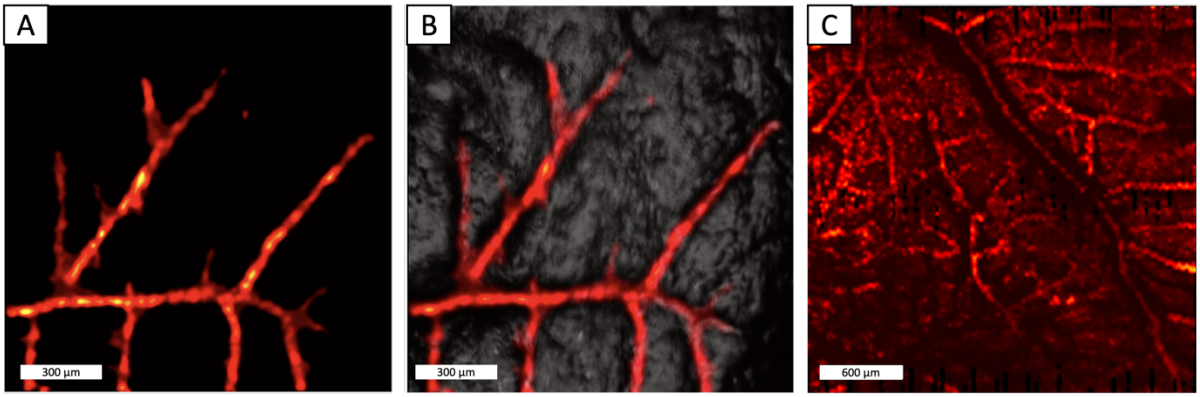

Figure 4-9. Chick embryo blood vessel images acquired using WFOV PARS microscopy. A. FOV is 1670 x 1670 µm^2. B. The blood vessel image in (A) overlayed onto a scattering image of the same area. C. FOV is 3340 x 3340 µm^2

Further development of the system is necessary to improve resolution, maximize FOV for *in-vivo* imaging, and speed up image acquisition. This potentially can be realized by integrating adaptive optics elements to actively correct for system- and specimen-induced aberration, adjust focus and address other issues of the system. A pinhole could also be added to the detection path before the photodiode to reduce noise coming from out-of-plane structures. Finally, a customized scan lens may be designed to improve system performance.

4.4 Conclusions

In summary, the design and evaluation of WFOV PARS microscopy that does not rely on mechanical scanning was reported. It has been demonstrated to capture images of leaf vein skeletons with a FOV of 11.9×11.9 mm^2 using its scattering mode and 8.5×8.5 mm^2 of carbon fibers using PARS. Furthermore, *in-vivo* studies were conducted on chick embryo CAM and blood vessel networks with the maximal FOV of 3.34 by 3.34 mm^2. Even though the system still requires further enhancements,

this study represents the first feasibility study toward fast purely optical WFOV PARS microscopy that is suitable for regular and agitation-sensitive samples.

Chapter 5: Conclusion and future work

In the first part of this thesis dissertation, a MEMS DM was integrated into PARS microscopy for depth scanning of biological tissues. The technique utilizes the defocus mode of the DM and optically shifts the focal plane. Optical axial scanning is a better alternative to mechanical axial scanning as it allows for faster imaging speed, doesn't agitate sensitive samples, and does not introduce motion artifacts. First, Zemax software was utilized to design the system and predict the focal shift. The calculated focal shift is 200 μm at 200 V of actuation. The focus shifting capability of the DM based PARS was then demonstrated using 1951 USAF targets and was found to be 240 μm at 300 V. Next, we imaged two layers of carbon fibers separated by a 151 μm thick cover glass. Moving the focal plane from the top layer to the bottom layer of carbon fibers was performed by changing the mirror shape. Finally, we used the DM-based PARS system to conduct depth scanning experiments in chick embryo CAM models by imaging blood vessels *in-vivo*.

Using the technology, rapid, high-resolution volumetric imaging of biological tissues can be performed with no contact, no labels, and reduced aberrations. A wide range of applications can be explored with DM-based PARS microscopy, including brain imaging, tumor angiogenesis, and multiwavelength studies.

Future work will focus on optimizing the speed of the DM-based PARS system so that rapid depth scanning can be achieved by automating the phase angle change. Increased beam diameter and the use of the full aperture of the objective lens will also enhance the resolution of the system. These improvements will allow for better visualization of capillaries and red blood cells. It will also be possible to correct chromatic shift due to wavelength changes in multiwavelength applications, such as oxygen saturation studies, by optically shifting the focal plane. Aberration correction applications can

also be performed with other modes of the deformable mirror. The primary spherical mode of the deformable mirror can be used in ophthalmology applications to correct spherical aberrations.

In the second part of this work, we described the design, construction, and assessment of optical scanning-based WFOV PARS microscopy. First, we conducted experiments to image 11.9×11.9 mm^2 wide leaf vein skeletons using the 830-nm scattering mode of the system. Next, we obtained 8.5×8.5 mm^2 wide images of carbon fiber network using PARS microscopy. Lastly, *in-vivo* experiments were conducted by imaging chick embryo CAM's vasculature with a maximum FOV of 3.34 by 3.34 mm^2. This study represents an early stage of development of the rapid and high-resolution WFOV PARS microscopy suitable for agitation-sensitive samples.

For better resolution, a wider field of view, and faster acquisition times, further development of the system is necessary. Integrating adaptive optics elements can potentially actively correct for system and specimen-induced aberrations, adjust focus, and address other system-related issues. In addition, it is possible to reduce noise from out-of-plane structures by adding a pinhole before the photodiode. The performance of a system can also be improved by designing a customized scan lens.

References

[1] J. C. Hebden, S. R. Arridge, and D. T. Delpy, "Optical imaging in medicine: I. Experimental techniques," *Phys Med Biol*, vol. 42, no. 5, pp. 825–840, May 1997, doi: 10.1088/0031-9155/42/5/007.

[2] J. A. Kubby, *Adaptive optics for biological imaging*. CRC Press, 2013.

[3] M. J. Booth, "Adaptive optics in microscopy," *Philosophical Transactions of the Royal Society A: Mathematical, Physical and Engineering Sciences*, vol. 365, no. 1861. Royal Society, pp. 2829–2843, Dec. 15, 2007. doi: 10.1098/rsta.2007.0013.

[4] "Introduction to Adaptive Optics and Deformable Mirrors." https://www.edmundoptics.com/knowledge-center/application-notes/optics/introduction-to-adaptive-optics-and-deformable-mirrors/#:%7E:text=Adaptive%20optics%20(AO)%20is%20a,by%20manipulating%20the%20optical%20wavefront.&text=This%20is%20why%20adaptive%20optics,quality%20or%20shape%20laser%20beams (accessed Jul. 05, 2022).

[5] H. W. Babcock, M. Wilson, and P. Observatories, "THE POSSIBILITY OF COMPENSATING ASTRONOMICAL SEEING," *Publications of the Astronomical Society of the Pacific*, vol. 65, no. 386, p. 229, Oct. 1953, doi: 10.1086/126606.

[6] F. Rigaut, "Astronomical Adaptive Optics," *Publications of the Astronomical Society of the Pacific*, vol. 127, no. 958, pp. 1197–1203, Jul. 2015, doi: 10.1086/684512.

[7] J. M. Geary, "Introduction to Wavefront Sensors," *Introduction to Wavefront Sensors*, 1995, doi: 10.1117/3.179559.

[8] M. Aftab, H. Choi, R. Liang, and D. W. Kim, "Adaptive Shack-Hartmann wavefront sensor accommodating large wavefront variations," *Opt Express*, vol. 26, no. 26, pp. 34428–34441, 2018, doi: 10.1364/OE.26.034428.

[9] "File:Shear-plate sideview with English text.png - Wikimedia Commons." https://commons.wikimedia.org/w/index.php?curid=106932751 (accessed Jul. 20, 2022).

[10] P. S. Salter and M. J. Booth, "Adaptive optics in laser processing," *Light: Science & Applications 2019 8:1*, vol. 8, no. 1, pp. 1–16, Nov. 2019, doi: 10.1038/s41377-019-0215-1.

[11] A. Jullien, "Photoniques 101 I", doi: 10.1051/photon/202010159.

[12] T. Review, "Adaptive Optics," *SpringerReference*, vol. 31, no. 9, 2011, doi: 10.1007/springerreference_7702.

[13] T. Bifano, "MEMS deformable mirrors," *Nature Photonics 2011 5:1*, vol. 5, no. 1, pp. 21–23, 2011, doi: 10.1038/nphoton.2010.297.

[14] G. Vdovin, M. Loktev, and A. Simonov, "Low-cost deformable mirrors: technologies and goals," in *Proc.SPIE*, Aug. 2005, vol. 5894. doi: 10.1117/12.621042.

[15] M. X. Hsieh, Y. F. Chen, Y. H. Hsieh, Y. H. Lai, and Y. T. Yu, “Integral-based parallel algorithm for the fast generation of the Zernike polynomials,” *Optics Express, Vol. 28, Issue 2, pp. 936-947*, vol. 28, no. 2, pp. 936–947, Jan. 2020, doi: 10.1364/OE.380567.

[16] P. Hajireza, W. Shi, K. Bell, R. J. Paproski, and R. J. Zemp, “Non-interferometric photoacoustic remote sensing microscopy,” *Light Sci Appl*, vol. 6, no. 6, pp. e16278–e16278, 2017, doi: 10.1038/lsa.2016.278.

[17] J. Yao and L. V Wang, “Photoacoustic microscopy,” *Laser Photon Rev*, vol. 7, no. 5, pp. 758–778, 2013, doi: https://doi.org/10.1002/lpor.201200060.

[18] P. Beard, “Biomedical photoacoustic imaging,” *Interface Focus*, vol. 1, no. 4, pp. 602–631, 2011, doi: 10.1098/rsfs.2011.0028.

[19] H. F. Zhang, K. Maslov, M.-L. Li, G. Stoica, and L. v Wang, “In vivo volumetric imaging of subcutaneous microvasculature by photoacoustic microscopy,” *Opt. Express*, vol. 14, no. 20, pp. 9317–9323, Oct. 2006, doi: 10.1364/OE.14.009317.

[20] Z. Hosseinaee, M. Le, K. Bell, and P. H. Reza, “Towards non-contact photoacoustic imaging [review],” *Photoacoustics*, vol. 20, p. 100207, Dec. 2020, doi: 10.1016/J.PACS.2020.100207.

[21] H. F. Zhang, C. A. Puliafito, and S. Jiao, “Photoacoustic Ophthalmoscopy for In Vivo Retinal Imaging: Current Status and Prospects,” *Ophthalmic Surg Lasers Imaging*, vol. 42, no. 0, p. S106, 2011, doi: 10.3928/15428877-20110627-10.

[22] A. de la Zerda *et al.*, “Photoacoustic ocular imaging,” *Opt Lett*, vol. 35, no. 3, p. 270, Feb. 2010, doi: 10.1364/OL.35.000270.

[23] P. H. Reza, K. Bell, W. Shi, J. Shapiro, and R. J. Zemp, “Deep non-contact photoacoustic initial pressure imaging,” *Optica, Vol. 5, Issue 7, pp. 814-820*, vol. 5, no. 7, pp. 814–820, Jul. 2018, doi: 10.1364/OPTICA.5.000814.

[24] S. Abbasi *et al.*, “Chromophore selective multi-wavelength photoacoustic remote sensing of unstained human tissues,” *Biomedical Optics Express, Vol. 10, Issue 11, pp. 5461-5469*, vol. 10, no. 11, pp. 5461–5469, Nov. 2019, doi: 10.1364/BOE.10.005461.

[25] S. Abbasi *et al.*, “All-optical Reflection-mode Microscopic Histology of Unstained Human Tissues,” *Scientific Reports 2019 9:1*, vol. 9, no. 1, pp. 1–11, Sep. 2019, doi: 10.1038/s41598-019-49849-9.

[26] K. Bell, K. Bell, L. Mukhangaliyeva, L. Khalili, and P. H. Reza, “Hyperspectral absorption microscopy using photoacoustic remote sensing,” *Optics Express, Vol. 29, Issue 15, pp. 24338-24348*, vol. 29, no. 15, pp. 24338–24348, Jul. 2021, doi: 10.1364/OE.430403.

[27] M. Boktor *et al.*, “Virtual histological staining of label-free total absorption photoacoustic remote sensing (TA-PARS),” *Scientific Reports 2022 12:1*, vol. 12, no. 1, pp. 1–12, Jun. 2022, doi: 10.1038/s41598-022-14042-y.

[28] Z. Hosseinaee *et al.*, “Functional and structural ophthalmic imaging using noncontact multimodal photoacoustic remote sensing microscopy and optical coherence tomography,” *Scientific Reports* |, vol. 11, p. 11466, 123AD, doi: 10.1038/s41598-021-90776-5.

[29] S. Abbasi, K. Bell, B. Ecclestone, and P. H. Reza, “Live feedback and 3D photoacoustic remote sensing,” *Quant Imaging Med Surg*, vol. 11, no. 3, pp. 1033–1045, Mar. 2021, doi: 10.21037/QIMS-20-758.

[30] B. R. Ecclestone *et al.*, “Three-dimensional virtual histology in unprocessed resected tissues with photoacoustic remote sensing (PARS) microscopy and optical coherence tomography (OCT),” *Scientific Reports* |, vol. 11, p. 13723, 123AD, doi: 10.1038/s41598-021-93222-8.

[31] J. W. O’BYRNE *et al.*, “ADAPTIVE OPTICS IN CONFOCAL MICROSCOPY,” pp. 85–90, Dec. 1999, doi: 10.1142/9789812817815_0014.

[32] M. J. Booth, M. A. A. Neil, R. Juškaitis, and T. Wilson, “Adaptive aberration correction in a confocal microscope,” *Proc Natl Acad Sci U S A*, vol. 99, no. 9, pp. 5788–5792, Apr. 2002, doi: 10.1073/PNAS.082544799/ASSET/75604EBF-C8D1-4874-9D19-EF7472F3BCE9/ASSETS/GRAPHIC/PQ0925447005.JPEG.

[33] L. Sherman, J. Y. Ye, O. Albert, and T. B. Norris, “Adaptive correction of depth-induced aberrations in multiphoton scanning microscopy using a deformable mirror,” *J Microsc*, vol. 206, no. 1, pp. 65–71, Apr. 2002, doi: 10.1046/J.1365-2818.2002.01004.X.

[34] P. N. Marsh, D. Burns, J. M. Girkin, D. S. Wan, M. Rajadhyaksha, and R. H. Webb, “Practical implementation of adaptive optics in multiphoton microscopy,” *Optics Express, Vol. 11, Issue 10, pp. 1123-1130*, vol. 11, no. 10, pp. 1123–1130, May 2003, doi: 10.1364/OE.11.001123.

[35] M. A. A. Neil, R. Juškaitis, M. J. Booth, T. Wilson, T. Tanaka, and S. Kawata, “Adaptive aberration correction in a two-photon microscope,” *J Microsc*, vol. 200, no. 2, pp. 105–108, Nov. 2000, doi: 10.1046/J.1365-2818.2000.00770.X.

[36] K. Yamaguchi *et al.*, “Adaptive Optical Two-Photon Microscopy for Surface-Profiled Living Biological Specimens,” *ACS Omega*, vol. 6, no. 1, pp. 438–447, Jan. 2021, doi: 10.1021/ACSOMEGA.0C04888/ASSET/IMAGES/LARGE/AO0C04888_0007.JPEG.

[37] B. Hermann *et al.*, “Adaptive-optics ultrahigh-resolution optical coherence tomography,” *Optics Letters, Vol. 29, Issue 18, pp. 2142-2144*, vol. 29, no. 18, pp. 2142–2144, Sep. 2004, doi: 10.1364/OL.29.002142.

[38] K. S. K. Wong, Y. Jian, M. Cua, S. Bonora, R. J. Zawadzki, and M. v Sarunic, “In vivo imaging of human photoreceptor mosaic with wavefront sensorless adaptive optics optical coherence tomography,” *Biomed Opt Express*, vol. 6, no. 2, pp. 580–590, 2015, doi: 10.1364/BOE.6.000580.

[39] A. J. Thompson, C. Paterson, C. Dunsby, M. A. A. Neil, and P. M. W. French, “Adaptive phase compensation for ultracompact laser scanning endomicroscopy,” *Optics Letters, Vol. 36, Issue 9, pp. 1707-1709*, vol. 36, no. 9, pp. 1707–1709, May 2011, doi: 10.1364/OL.36.001707.

[40] F. Bortoletto, C. Bonoli, P. Panizzolo, C. D. Ciubotaru, and F. Mammano, “Multiphoton Fluorescence Microscopy with GRIN Objective Aberration Correction by Low Order Adaptive Optics,” *PLoS One*, vol. 6, no. 7, p. e22321, 2011, doi: 10.1371/JOURNAL.PONE.0022321.

[41] O. Azucena *et al.*, “Adaptive optics wide-field microscopy using direct wavefront sensing,” *Optics Letters, Vol. 36, Issue 6, pp. 825-827*, vol. 36, no. 6, pp. 825–827, Mar. 2011, doi: 10.1364/OL.36.000825.

[42] P. Vermeulen, E. Muro, T. Pons, V. Loriette, and A. Fragola, “Adaptive optics for fluorescence wide-field microscopy using spectrally independent guide star and markers,” *https://doi.org/10.1117/1.3603847*, vol. 16, no. 7, p. 076019, Jul. 2011, doi: 10.1117/1.3603847.

[43] O. Azucena *et al.*, “Wavefront aberration measurements and corrections through thick tissue using fluorescent microsphere reference beacons,” *Optics Express, Vol. 18, Issue 16, pp. 17521-17532*, vol. 18, no. 16, pp. 17521–17532, Aug. 2010, doi: 10.1364/OE.18.017521.

[44] M. R. Reinig *et al.*, “Adaptive optics microscopy enhances image quality in deep layers of CLARITY processed brains of YFP-H mice,” *SPIE*, vol. 9690, p. 969008, Mar. 2016, doi: 10.1117/12.2213283.

[45] K. Wang *et al.*, “Rapid adaptive optical recovery of optimal resolution over large volumes,” *Nature Methods 2014 11:6*, vol. 11, no. 6, pp. 625–628, Apr. 2014, doi: 10.1038/nmeth.2925.

[46] N. Ji, T. R. Sato, and E. Betzig, “Characterization and adaptive optical correction of aberrations during in vivo imaging in the mouse cortex,” *Proc Natl Acad Sci U S A*, vol. 109, no. 1, pp. 22–27, Jan. 2012, doi: 10.1073/PNAS.1109202108/SUPPL_FILE/SM02.AVI.

[47] J. Li *et al.*, “Study on Aberration Correction of Adaptive Optics Based on Convolutional Neural Network,” *Photonics 2021, Vol. 8, Page 377*, vol. 8, no. 9, p. 377, Sep. 2021, doi: 10.3390/PHOTONICS8090377.

[48] “Dynamic and Agile Focusing in Microscopy: A Review,” *https://doi.org/10.1117/3.2248542.ch1*, vol. SL20, pp. 1–36, Aug. 2016, doi: 10.1117/3.2248542.CH1.

[49] G. Lan *et al.*, “Design of high-performance adaptive objective lens with large optical depth scanning range for ultrabroad near infrared microscopic imaging,” *Biomedical Optics Express, Vol. 6, Issue 9, pp. 3362-3377*, vol. 6, no. 9, pp. 3362–3377, Sep. 2015, doi: 10.1364/BOE.6.003362.

[50] Y.-H. Lin, H.-S. Chen, M.-S. Chen Yi-Hsin Lin, and M.-S. Chen, “Electrically-tunable liquid crystal lenses and applications,” *https://doi.org/10.1117/12.2005580*, vol. 8642, no. 5, pp. 65–76, Mar. 2013, doi: 10.1117/12.2005580.

[51] A. Solodar, I. Klapp, and I. Abdulhalim, “Annular liquid crystal spatial light modulator for beam shaping and extended depth of focus,” *Opt Commun*, vol. 323, pp. 167–173, Jul. 2014, doi: 10.1016/J.OPTCOM.2014.02.066.

[52] A. Bagramyan, T. Galstian, and A. Saghatelyan, “Motion-free endoscopic system for brain imaging at variable focal depth using liquid crystal lenses,” *J Biophotonics*, vol. 10, no. 6–7, pp. 762–774, Jun. 2017, doi: 10.1002/JBIO.201500261.

[53] K. Asatryan, A. Tork, A. Bagramyan, A. Zohrabyan, T. Galstian, and V. Presnyakov, “Optical lens with electrically variable focus using an optically hidden dielectric structure,” *Optics Express, Vol. 18, Issue 13, pp. 13981-13992*, vol. 18, no. 13, pp. 13981–13992, Jun. 2010, doi: 10.1364/OE.18.013981.

[54] O. Sova, T. Asatryan, KarenGalstian, and V. Reshetnyak, “Electrically variable liquid crystal lens based on the dielectric dividing principle,” *JOSA A, Vol. 32, Issue 5, pp. 803-808*, vol. 32, no. 5, pp. 803–808, May 2015, doi: 10.1364/JOSAA.32.000803.

[55] N. T. Nguyen, “Micro-optofluidic Lenses: A review,” *Biomicrofluidics*, vol. 4, no. 3, 2010, doi: 10.1063/1.3460392.

[56] U. Levy and R. Shamai, “Tunable optofluidic devices,” *Microfluidics and Nanofluidics 2007 4:1*, vol. 4, no. 1, pp. 97–105, Sep. 2007, doi: 10.1007/S10404-007-0216-X.

[57] K. F. Tehrani, M. K. Sun, L. Karumbaiah, and L. J. Mortensen, “Fast axial scanning for 2-photon microscopy using liquid lens technology,” *Proc SPIE Int Soc Opt Eng*, vol. 10070, p. 100700Y, Mar. 2017, doi: 10.1117/12.2252992.

[58] A. Doblas *et al.*, “Three-dimensional microscopy through liquid-lens axial scanning,” *https://doi.org/10.1117/12.2177680*, vol. 9495, p. 949503, May 2015, doi: 10.1117/12.2177680.

[59] L. Dong, A. K. Agarwal, D. J. Beebe, and H. Jiang, “Adaptive liquid microlenses activated by stimuli-responsive hydrogels,” *Nature 2006 442:7102*, vol. 442, no. 7102, pp. 551–554, Aug. 2006, doi: 10.1038/nature05024.

[60] A. Peinado, E. A. Bendek, S. Yokoyama, and K. E. Poskanzer, “Deformable mirror-based axial scanning for two-photon mammalian brain imaging,” *https://doi.org/10.1117/1.NPh.8.1.015003*, vol. 8, no. 1, p. 015003, Jan. 2021, doi: 10.1117/1.NPH.8.1.015003.

[61] A. Roorda, “Applications of adaptive optics scanning laser ophthalmoscopy,” *Optometry and Vision Science*, vol. 87, no. 4, pp. 260–268, Apr. 2010, doi: 10.1097/OPX.0B013E3181D39479.

[62] Y. Gong *et al.*, “High-speed recording of neural spikes in awake mice and flies with a fluorescent voltage sensor,” *Science (1979)*, vol. 350, no. 6266, pp. 1361–1366, Dec. 2015, doi: 10.1126/SCIENCE.AAB0810/SUPPL_FILE/GONG-SM.PDF.

[63] P. Carmeliet and R. K. Jain, “Angiogenesis in cancer and other diseases,” *Nature 2000 407:6801*, vol. 407, no. 6801, pp. 249–257, Sep. 2000, doi: 10.1038/35025220.

[64] L. Nie *et al.*, “In Vivo Volumetric Photoacoustic Molecular Angiography and Therapeutic Monitoring with Targeted Plasmonic Nanostars,” *Small*, vol. 10, no. 8, pp. 1585–1593, Apr. 2014, doi: 10.1002/SMLL.201302924.

[65] S. Kocer *et al.*, “Resonant Varifocal Mems Mirror,” in *2022 IEEE 35th International Conference on Micro Electro Mechanical Systems Conference (MEMS)*, 2022, pp. 963–966. doi: 10.1109/MEMS51670.2022.9699771.

[66] S. Kocer, “Resonant MEMS Deformable Mirror,” *UWSpace*, 2022. https://uwspace.uwaterloo.ca/handle/10012/17939 (accessed Apr. 19, 2022).

[67] M. Naik, P. Brahma, and M. Dixit, “A Cost-Effective and Efficient Chick Ex-Ovo CAM Assay Protocol to Assess Angiogenesis.,” *Methods Protoc*, vol. 1, no. 2, May 2018, doi: 10.3390/mps1020019.

[68] G. Recher, P. Nassoy, and A. Badon, “Remote scanning for ultra-large field of view in wide-field microscopy and full-field OCT,” *Biomedical Optics Express, Vol. 11, Issue 5, pp. 2578-2590*, vol. 11, no. 5, pp. 2578–2590, May 2020, doi: 10.1364/BOE.383329.

[69] B. Potsaid, J. T. Wen, and Y. Bellouard, “Adaptive Scanning Optical Microscope (ASOM): A multidisciplinary optical microscope design for large field of view and high resolution imaging,” *Optics Express, Vol. 13, Issue 17, pp. 6504-6518*, vol. 13, no. 17, pp. 6504–6518, Aug. 2005, doi: 10.1364/OPEX.13.006504.

[70] C. Bechtel, J. Knobbe, H. Grüger, and H. Lakner, “Large field of view MEMS-based confocal laser scanning microscope for fluorescence imaging,” *Optik (Stuttg)*, vol. 125, no. 2, pp. 876–882, 2014, doi: https://doi.org/10.1016/j.ijleo.2013.07.091.

[71] P. S. Tsai, C. Mateo, J. J. Field, C. B. Schaffer, M. E. Anderson, and D. Kleinfeld, “Ultra-large field-of-view two-photon microscopy,” *Opt Express*, vol. 23, no. 11, pp. 13833–13847, 2015, doi: 10.1364/OE.23.013833.

[72] F. Atry and R. Pashaie, “Analysis of intermediary scan-lens and tube-lens mechanisms for optical coherence tomography,” *Appl Opt*, vol. 55, no. 4, pp. 646–653, 2016, doi: 10.1364/AO.55.000646.

[73] M. T. Martell, N. J. M. Haven, and R. J. Zemp, “Multimodal imaging with spectral-domain optical coherence tomography and photoacoustic remote sensing microscopy,” *Opt Lett*, vol. 45, no. 17, pp. 4859–4862, 2020, doi: 10.1364/OL.398940.